LJMU Research Online

Loveday, J, Christodoulou, L, Norberg, P, Peacock, JA, Baldry, IK, Bland-Hawthorn, J, Brown, MJI, Colless, M, Driver, SP, Holwerda, BW, Hopkins, AM, Kafle, PR, Liske, J, Lopez-Sanchez, AR and Taylor, EN

 Galaxy and Mass Assembly (GAMA): Small-scale anisotropic galaxy clustering and the pairwise velocity dispersion of galaxies

http://researchonline.ljmu.ac.uk/id/eprint/7698/

Article

Galaxy and Mass Assembly (GAMA): small-scale anisotropic galaxy clustering and the pairwise velocity dispersion of galaxies

J. Loveday,[1]⋆ L. Christodoulou,[1] P. Norberg,[2] J. A. Peacock,[3] I. K. Baldry,[4] J. Bland-Hawthorn,[5] M. J. I. Brown,[6] M. Colless,[7] S. P. Driver,[8,9] B. W. Holwerda,[10] A. M. Hopkins,[11] P. R. Kafle,[8] J. Liske,[12] A. R. Lopez-Sanchez[11,13] and E. N. Taylor[14]

[1]*Astronomy Centre, University of Sussex, Falmer, Brighton BN1 9QH, UK*
[2]*ICC & CEA, Department of Physics, Durham University, South Road, Durham DH1 3LE, UK*
[3]*Institute for Astronomy, University of Edinburgh, Royal Observatory, Blackford Hill, Edinburgh EH9 3HJ, UK*
[4]*Astrophysics Research Institute, Liverpool John Moores University, IC2, Liverpool Science Park, 146 Brownlow Hill, Liverpool, L3 5RF, UK*
[5]*Sydney Institute for Astronomy, School of Physics, University of Sydney, Sydney, NSW 2006, Australia*
[6]*School of Physics, Monash University, Clayton, Victoria 3800, Australia*
[7]*Research School of Astronomy & Astrophysics, The Australian National University, Cotter Road, Weston Creek, ACT 2611, Australia*
[8]*International Centre for Radio Astronomy Research (ICRAR), The University of Western Australia, 35 Stirling Highway, Crawley, WA6009, Australia*
[9]*School of Physics & Astronomy, University of St Andrews, North Haugh, St Andrews, KY16 9SS, UK*
[10]*Department of Physics and Astronomy, University of Louisville, Louisville, KY 40292, USA*
[11]*Australian Astronomical Observatory, PO Box 915, North Ryde, NSW 1670, Australia*
[12]*European Southern Observatory, Karl-Schwarzschild-Str. 2, D-85748 Garching, Germany*
[13]*Department of Physics and Astronomy, Macquarie University, Sydney, NSW 2109, Australia*
[14]*Centre for Astrophysics & Supercomputing, Swinburne University of Technology, PO Box 218, Hawthorn, VIC 3122, Australia*

ABSTRACT

The galaxy pairwise velocity dispersion (PVD) can provide important tests of non-standard gravity and galaxy formation models. We describe measurements of the PVD of galaxies in the Galaxy and Mass Assembly (GAMA) survey as a function of projected separation and galaxy luminosity. Due to the faint magnitude limit ($r < 19.8$) and highly complete spectroscopic sampling of the GAMA survey, we are able to reliably measure the PVD to smaller scales ($r_\perp = 0.01\, h^{-1}$ Mpc) than previous work. The measured PVD at projected separations $r_\perp \lesssim 1\, h^{-1}$ Mpc increases near monotonically with increasing luminosity from $\sigma_{12} \approx 200\,\mathrm{km\,s^{-1}}$ at $M_r = -17$ mag to $\sigma_{12} \approx 600\,\mathrm{km\,s^{-1}}$ at $M_r \approx -22$ mag. Analysis of the Gonzalez-Perez et al. (2014) GALFORM semi-analytic model yields no such trend of PVD with luminosity: the model overpredicts the PVD for faint galaxies. This is most likely a result of the model placing too many low-luminosity galaxies in massive haloes.

Key words: galaxies: kinematics and dynamics – galaxies: statistics.

1 INTRODUCTION

The pairwise velocity dispersion (PVD, σ_{12}), the dispersion in relative peculiar velocity of galaxy pairs, has an illustrious history in observational cosmology. It was first measured in 1973 by Geller & Peebles (1973), and soon became popular as a way of estimating the mean mass density of the Universe, Ω_m, via the cosmic virial theorem or cosmic energy equation (e.g. Peebles 1976a,b, 1979; Bean et al. 1983; Davis & Peebles 1983; Bartlett & Blanchard 1996). In fact, these measurements provided perhaps the first evidence that we live in a Universe which has a sub-critical mass density, $\Omega_m < 1$.

Use of the PVD to constrain cosmological parameters then fell out of favour, largely due to its sensitivity to the presence or absence of rich clusters in the survey data used (Mo, Jing & Borner 1993).

Nevertheless, knowledge of the (non-linear) PVD is required when modelling the linear, large-scale Kaiser (1987) infall in order to constrain the growth rate of structure (e.g. Peacock et al. 2001; Guzzo et al. 2008; Blake et al. 2013). The PVD is an important quantity for modelling the galaxy redshift–space correlation function, and can be used to test predictions of galaxy formation and evolution models, the focus of this paper, and of the cold dark matter paradigm in general.

Recently, interest in use of the PVD as a cosmological diagnostic has been reawakened, both due to the availability of large spectroscopic surveys which encompass fair samples of the

⋆ E-mail: J.Loveday@sussex.ac.uk

Universe, and due to theoretical developments in modified gravity. There have been several recent efforts to model modified gravity using N-body simulations, allowing one to compare the predictions of small-scale galaxy dynamics (e.g. Fontanot et al. 2013; Falck et al. 2015; Winther et al. 2015; Bibiano & Croton 2017). In particular, Hellwing et al. (2014) have shown that the PVD provides one of the most sensitive diagnostics of modified gravity, with some of these models predicting dispersions about 30 per cent larger or smaller than General Relativity.

Since the first measurements of Geller & Peebles (1973), the PVD has been measured for most redshift surveys (e.g. Bean et al. 1983; Davis & Peebles 1983; Loveday et al. 1996; Jing et al. 1998; Jing & Borner 2001a; Landy 2002; Zehavi et al. 2002; Hawkins et al. 2003; Jing & Borner 2004; Li et al. 2006; Van Den Bosch et al. 2007; Cabré & Gaztañaga 2009). Predictions of the PVD from halo occupation distribution (HOD) models and/or simulations have been made by Slosar, Seljak & Tasitsiomi (2006), Li et al. (2007), Tinker et al. (2007) and Van Den Bosch et al. (2007). A good summary of previous results for the overall PVD, i.e. measured over all galaxy types and a wide range of scales, is provided by Landy (2002). Most estimates range from around 300 to 600 km s^{-1}, and are sensitive to the presence or absence of rich clusters in the data used (Mo et al. 1993). The advent of large redshift surveys, such as the two-degree Field Galaxy Redshift Survey (2dFGRS; Colless et al. 2001) and the Sloan Digital Sky Survey (SDSS; York et al. 2000), enabled detailed studies of the dependence of the PVD on galaxy type and scale. Hawkins et al. (2003) measure the PVD for 2dFGRS galaxies, finding a peak $\sigma_{12} \approx 600$ km s^{-1} at projected separations $r_\perp \approx 0.2$–0.8 h^{-1} Mpc, with σ_{12} declining to 300–400 km s^{-1} at smaller and larger scales, consistent with contemporary semi-analytic model predictions. Jing & Borner (2004) find that at a scale of $k = 1\,h\,\mathrm{Mpc}^{-1}$, the 2dFGRS PVD has a minimum value of $\sigma_{12} \approx 400$ km s^{-1} for galaxies of luminosity $M^* - 1$, increasing rapidly for both fainter and brighter galaxies. Li et al. (2006) measure the PVD for SDSS galaxies as a function of luminosity and stellar mass as well as other galaxy properties. Consistent with Jing & Borner (2004), they find that the PVD measured at $k = 1\,h\,\mathrm{Mpc}^{-1}$ has a minimum value of $\sigma_{12} \approx 500$ km s^{-1} for galaxy luminosities around $M^* - 1$, increasing somewhat for less luminous galaxies, and markedly (to $\sigma_{12} \approx 700$ km s^{-1}) for the most luminous galaxies in the sample. They also find that red galaxies have systematically higher PVDs than blue galaxies, particularly for less luminous galaxies. In a followup paper, Li et al. (2007) compare the clustering and PVD of SDSS galaxies with semi-analytic models, finding that the models overpredict the clustering strength and PVD for sub-L^* galaxies, particularly at small scales.

The Galaxy and Mass Assembly (GAMA) survey (Driver et al. 2011) provides an ideal opportunity for a new measurement of the PVD due to (i) being two magnitudes fainter than the SDSS main galaxy sample, and (ii) having very high (>98 per cent) spectroscopic completeness, even in high-density regions. The latter point means that completeness corrections for 'fibre collisions' are not an issue with GAMA data. We utilize the three equatorial regions in GAMA-II (Liske et al. 2015), covering a total area of 180 deg^2, and including galaxies down to Petrosian r-band apparent magnitude $r = 19.8$. The GAMA-II data base has previously been used to measure the projected galaxy clustering in bins of stellar mass and luminosity (Farrow et al. 2015) and to measure the growth rate of large-scale structure via linear-regime redshift-space distortions (RSD) (Blake et al. 2013). Here, we focus on measuring RSD in the non-linear regime, $r_\perp \lesssim 10\,h^{-1}$ Mpc.

The paper is structured as follows. We discuss the GAMA data, mock and random catalogues in Section 2 and measurement of two-dimensional and projected correlation functions in Section 3. In Section 4, we describe two models for the redshift–space correlation function, and demonstrate that the pairwise velocity distribution function is close to exponential. We test three different ways of measuring the PVD using mock catalogues in Section 5. PVDs for the GAMA data in luminosity bins, along with a comparison of mock predictions, are shown in Section 6; we conclude in Section 7. Throughout, we assume a Hubble constant of $H_0 = 100\,h\,\mathrm{km\,s^{-1}\,Mpc^{-1}}$ and an $\Omega_M = 0.25$, $\Omega_\Lambda = 0.75$ cosmology in calculating distances, comoving volumes and luminosities. Uncertainties on all results from GAMA data and mocks are based on jackknife sampling and from the scatter between realizations, respectively.

2 DATA, MOCK AND RANDOM CATALOGUES

2.1 GAMA data

Our observed sample consists of galaxies from the GAMA-II equatorial regions G09, G12 and G15, each 5 × 12 deg in extent and 98 per cent spectroscopically complete to $r = 19.8$ mag (Liske et al. 2015). Specifically, galaxy coordinates and magnitudes come from TilingCatv46 (Baldry et al. 2010). Redshifts, corrected by the multi-attractor flow model of Tonry et al. (2000), as described by Baldry et al. (2012), are taken from DistancesFramesv14. K-corrections to reference redshift $z_0 = 0.1$ (Blanton & Roweis 2007) and fourth-order polynomial fits are obtained from kCorrectionsv05 (Loveday et al. 2012).

In order to estimate errors on our results, we subdivide each GAMA field into three 4 × 5 deg regions, and determine the covariance by omitting each of the nine jackknife regions in turn. The median velocity uncertainty in GAMA is 33 km s^{-1} (Baldry et al. 2014), significantly less than the smallest measured velocity dispersions, and so we quote PVDs uncorrected for these measurement errors. Similarly, we ignore the effect of blended galaxy spectra, where galaxies are either lensed or overlapping (Holwerda et al. 2015), since this affects only 0.05 per cent of the GAMA sample.

2.2 GALFORM mock catalogues

We compare our GAMA results with mock galaxy catalogues based on the Millennium-WMAP7 Simulation (Guo et al. 2013) and the Gonzalez-Perez et al. (2014) GALFORM model, with lightcones produced using the method of Merson et al. (2013); see Farrow et al. (2015) for further details of these GAMA mocks. Specifically, we queried the table GAMA_v1..LC_multi_Gonzalez2014a via the Durham-hosted Virgo-Millennium Database[1] (Lemson & the Virgo Consortium 2006).

We utilize 26 mock realizations of the three equatorial GAMA fields (G09, G12 and G15), selecting galaxies down to apparent SDSS r-band magnitude $r < 19.8$ mag. These mocks were extracted from the Millennium-WMAP7 simulation cube using random observer position and orientations. As such they are not independent, but do allow some assessment of sample variance. Since the mocks provide both an observed and a cosmological redshift, we can make a direct estimate of the PVD to compare with our clustering-based

---

[1] Millennium DB at http://virgodb.dur.ac.uk.

PVD estimators. Covariance estimates for the mocks come from comparing the 26 realizations. In practice, we use only the diagonal elements of the covariance matrix. Since we focus on the small-scale PVD, the relatively small number and lack of true independence of the mocks is not a serious issue.

2.3 Random catalogues

In order to account for the survey boundaries and selection effects, we generate random catalogues obeying the same mask and selection function as the GAMA data, but without clustering. The mask and selection function are derived independently from those of Farrow et al. (2015); we have checked that we obtain consistent results for the projected correlation function (see Appendix A). The mock catalogues have a simple mask corresponding to the RA–dec boundaries of the GAMA equatorial regions. The radial distribution of random points for analysing the mocks is obtained by taking the mock galaxy redshifts from all 26 realizations of the three GAMA fields; large-scale structure in individual realizations is rendered invisible in the combined distribution. The following subsections describe the survey mask and radial selection function for the GAMA data.
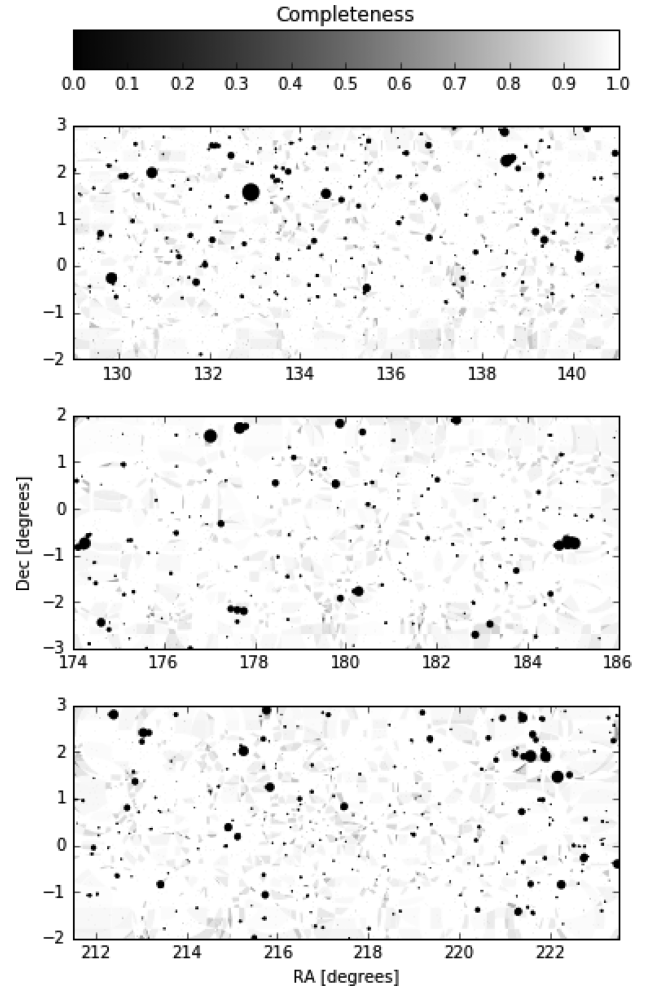
2.3.1 Survey mask

Since GAMA-II target selection was made from SDSS DR7 (Abazajian et al. 2009) *r*-band imaging, we mask out regions of *r*-band imaging identified by the SDSS photometric pipeline as any of BLEEDING, BRIGHT_STAR, TRAIL, HOLE[2]. In addition, we mask out areas around bright stars ($V < 12$ mag) in the *Tycho* and *Hipparcos* catalogues (see Baldry et al. 2010 for details).

In order to map spectroscopic completeness as a function of position on the sky, we obtain a list of GAMA 2dF field centres from the table AATFieldsv25. The (zero-weight) mask regions and (unit-weight) spectroscopic fields are then combined using the PIXELIZE, SNAP and BALKANIZE commands in MANGLE (Hamilton & Tegmark 2004; Swanson et al. 2008). The result is a list of polygons defined by overlap regions of the 2dF fields with masked regions set to zero weight. We then set the weight of each non-masked polygon to its spectroscopic completeness by dividing the number of main-survey targets (survey_class >3) with reliable redshifts ($nQ > 2$) by the number of targets within each polygon. Finally, we trim the polygons to lie within the equatorial coordinate ranges of the three GAMA regions, namely $\alpha = (129.0, 141.0), (174.0, 186.0), (211.5, 223.5), \delta = (-2.0, 3.0), (-3.0, 2.0), (-2.0, 3.0)$, for G09, G12 and G15, respectively. The resulting spectroscopic completeness maps are shown in Fig. 1. Angular coordinates of random points are generated using the MANGLE RANSACK command with density proportional to the completeness within each polygon.

2.3.2 Radial selection function

When analysing samples that are not volume-limited, the radial coordinates of random points are generated from each sample using the joint stepwise maximum likelihood (JSWML) method of Cole (2011), as adapted for use with GAMA by Loveday et al. (2015), assuming evolution parameters $P = Q = 1$.

For volume-limited samples, we distribute points drawn at random from a distribution uniform in comoving volume modulated by the density-evolution factor $10^{0.4Pz}$ (Loveday et al. 2015,

---

[2] See http://www.sdss.org/dr7/algorithms/masks.html.

Figure 1. Spectroscopic completeness mask for the GAMA-II regions. Black regions correspond to holes cut around bright stars and SDSS imaging defects.

equation 5). Limiting redshifts for each volume-limited sample are chosen such that the distribution of individual *K*-corrections for galaxies close to the limiting redshift results in a sample that is 95 per cent complete.

2.3.3 Comparison with previous GAMA clustering measurements

Since both the angular mask and radial selection function for the random catalogues have been derived independently from a previous measurement of galaxy clustering from the GAMA data (Farrow et al. 2015), we compare our clustering estimates for a number of galaxy subsamples in Appendix A. We find results that are in excellent agreement on all small scales.

2.4 Data subsamples

We measure the PVD of GAMA galaxies in bins of absolute magnitude, as summarized in Table 1. For all GAMA samples, we employ individual *K*-corrections to rest-frame $z = 0.1$ and assume luminosity evolution given by $Q = 1$ as described in Loveday et al. (2015). We use a superscript prefix of 0.1, $^{0.1}M_r$, to indicate an absolute magnitude *K*-corrected to a passband blueshifted by $z = 0.1$. This is done for the GAMA data to allow comparison with the results of Li et al. (2006). A superscript prefix of 0.0 indicates an absolute

Table 1. GAMA and mock galaxy subsamples. GAMA magnitudes are evolution-corrected $^{0.1}M_r$; mock magnitudes, $^{0.0}M_r$, are taken directly from the mock catalogues.

Name	GAMA mag	N_{gal}	Mock mag	N_{mock}
V0	$[-23, -20]$	41 757	$[-23, -20]$	$53\,878 \pm 3\,038$
M1	$[-23, -22]$	3 730	$[-23.47, -22.36]$	$3\,507 \pm 108$
M2	$[-22, -21]$	37 904	$[-22.36, -21.02]$	$38\,278 \pm 934$
M3	$[-21, -20]$	68 791	$[-21.02, -19.85]$	$67\,704 \pm 2\,468$
M4	$[-20, -19]$	43 105	$[-19.85, -18.19]$	$44\,115 \pm 2\,133$
M5	$[-19, -18]$	17 550	$[-18.19, -17.00]$	$17\,224 \pm 1\,570$
M6	$[-18, -17]$	6 037		
M7	$[-17, -16]$	2 080		
M8	$[-16, -15]$	805		

magnitude K-corrected to the rest-frame of the galaxy, as appropriate for the mock data.

Because the mocks do not provide an exact match to GAMA in terms of luminosity function, K-corrections and evolution, we cannot obtain a fair comparison by using the same magnitude limits. Instead, we select samples matched on number density, as is common in the literature (e.g. Berlind et al. 2003; Zheng et al. 2005; Contreras et al. 2013; Farrow et al. 2015).

Allowing for the fact that the GAMA mask removes about 0.7 per cent of the survey area (Baldry et al. 2010) and that the GAMA redshift incompleteness is about 1.5 per cent (Liske et al. 2015), one would expect the GAMA catalogues to contain about 2.5 per cent fewer galaxies than the mocks if they have the same underlying number density.[3] Starting with an absolute magnitude threshold of $^{0.1}M_r = -23$ mag, we count the number of GAMA galaxies brighter than this threshold within redshift $z < 0.65$. We find the corresponding mock absolute magnitude threshold that gives 1.025 times as many galaxies when averaged over the 26 mock realizations within the same redshift limit. This process is repeated for the remaining magnitude bins; the corresponding magnitude limits for the mocks are given in Table 1. Note that the GAMA magnitudes are K- and evolution-corrected to $z_0 = 0.1$, assuming luminosity evolution given by $Q = 1$, whereas we use absolute r-band magnitudes (SDSS_r_rest_abs) taken directly from the mock catalogue without any evolution correction. For sample M5, we set the mock faint magnitude limit to be -17 mag, even though this sample contains fewer galaxies than the corresponding GAMA sample. This is due to the resolution limit of the Millennium Simulation: samples fainter than $^{0.0}M_r \approx -17$ mag will be incomplete in a halo-dependent way. This incompleteness in the mock catalogues may explain the spuriously high clustering signal measured by Farrow et al. (2015, fig. 11) for the $-18 < {}^{0.0}M_r < -17$ mag mock sample.

For testing our methods in Sections 4 and 5, we employ a volume-limited sample (V0), with $^{0.1}M_r < -20$ mag and redshift $z < 0.258$. These limits are chosen in order to roughly maximize the number of galaxies in a volume-limited sample. We choose the same limits for the mocks, since number densities are very similar at this magnitude. While the corresponding redshift limit will not be identical for the mock catalogues, this is not an issue, as the random distribution for analysing mock galaxy clustering is generated from the mocks themselves.

---

[3] Although the GAMA regions are underdense with respect to SDSS by about 15 per cent within $z < 0.1$ (Driver et al. 2011), there is no evidence that this underdensity extends out to larger redshifts. The overall sample variance of GAMA is expected to be about 3 per cent (Driver & Robotham 2010).

The real-space correlation function for the V0 mock sample is well-fitted on scales $r \lesssim 16\,h^{-1}$ Mpc by a power law with $\gamma = 1.81$, $r_0 = 5.6\,h^{-1}$ Mpc. From numerical integration of this power law, we find that the variance of galaxy counts in $8\,h^{-1}$ Mpc radius spheres is very close to 1, $\sigma_{8,g}^2 \approx 0.98$. Since the simulations assume the WMAP7 cosmology ($\Omega_m = 0.272$, $\sigma_8 = 0.807$; Guo et al. 2013), the bias of this mock galaxy sample is $b = \sigma_{8,g}/\sigma_8 \approx 1.23$ and hence the expected value of the redshift space distortion parameter is given by $\beta = \Omega_m^{0.6}/b \approx 0.37$.

Our primary results (Section 6) show galaxies in non-volume-limited bins of luminosity (M1–M8), as well as five samples drawn from a single volume-limited sample.

3 MEASURING THE CORRELATION FUNCTION

Our measurements of the PVD are based on the two-dimensional galaxy correlation function $\xi(r_\perp, r_\parallel)$; the excess probability above random of finding two galaxies separated by $r_\parallel$ along the line of sight (LOS) and $r_\perp$ perpendicular to the LOS. These separations are calculated in the usual way (e.g. Fisher et al. 1994). Two galaxies with position vectors $\mathbf{r}_1$ and $\mathbf{r}_2$ are separated by vector $\mathbf{s} = \mathbf{r}_2 - \mathbf{r}_1$. For an observer at the origin, the vector to the midpoint of the pair is given by $\mathbf{l} = (\mathbf{r}_1 + \mathbf{r}_2)/2$. The LOS and perpendicular separations of the galaxies are then given by $r_\parallel = |\mathbf{s} \cdot \hat{\mathbf{l}}|$, with $\hat{\mathbf{l}}$ being the unit vector in the direction of $\mathbf{l}$, and $r_\perp = \sqrt{\mathbf{s} \cdot \mathbf{s} - r_\parallel^2}$.

To estimate $\xi(r_\perp, r_\parallel)$, we use the Landy & Szalay (1993) estimator,

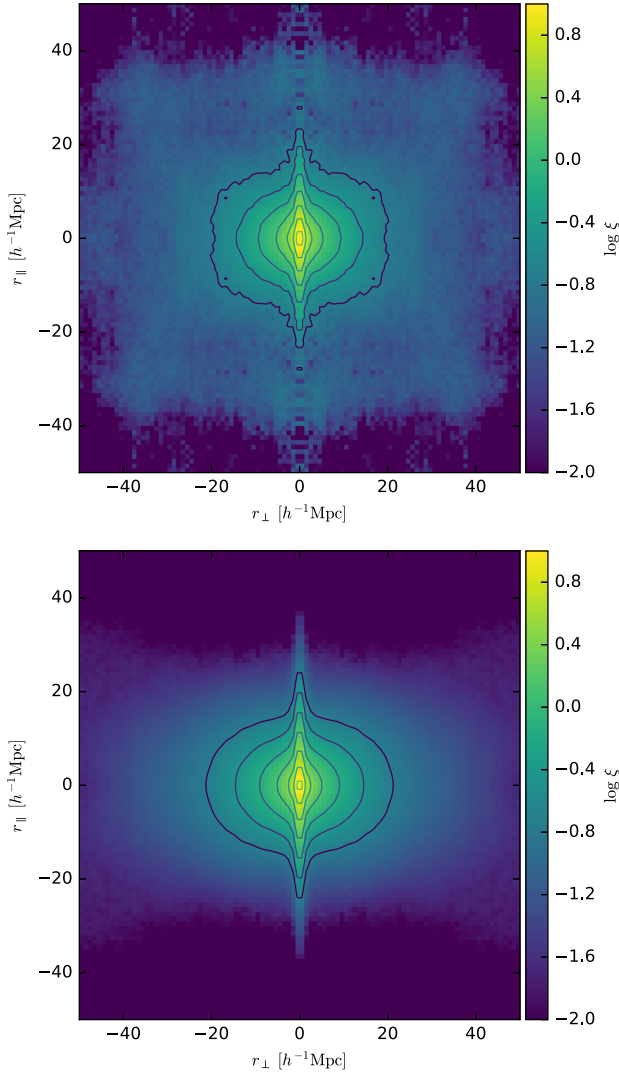$$\xi(r_\perp, r_\parallel) = \frac{DD - 2DR + RR}{RR}, \tag{1}$$

where DD, DR and RR are the normalized and weighted numbers of data–data, data–random and random–random, respectively, pairs in a given $(r_\perp, r_\parallel)$ bin. The random points are generated as described in the previous section. For non-volume-limited samples, the pair counts are weighted to allow for the declining selection function with redshift, giving a minimum-variance estimator (Hamilton 1993). Each galaxy pair is given a weight

$$w_{ij} = \{[1 + 4\pi\bar{n}(z_i)J_3(s_{ij})][1 + 4\pi\bar{n}(z_j)J_3(s_{ij})]\}^{-1}, \tag{2}$$

where $\bar{n}(z)$ is the average galaxy number density of the corresponding unclustered sample at the redshift of each galaxy, z_i and z_j, and $J_3(s_{ij}) = \int_0^{s_{ij}} s^2 \xi(s) ds$. For this integral, we assume a power law for the correlation function, $\xi(s) = (s/s_0)^{-\gamma}$, with parameters $s_0 = 5.59\,h^{-1}$ Mpc and $\gamma = 1.84$, and we integrate out to the separation s_{ij} of the galaxy pair, or $30\,h^{-1}$ Mpc, if the separation is larger than this. We have checked that the correlation function estimates are insensitive to the details of the assumed power law. If, instead, we assume a power law consistent with the clustering of GAMA galaxies in the faint magnitude bin M6, viz. $s_0 = 3.68\,h^{-1}$ Mpc, $\gamma = 1.84$, individual $w_p(r_\perp)$ estimates change by less than the 1σ error bars. For volume-limited samples, weighting is uniform, i.e. $w_{ij} \equiv 1$.

We then normalize for the relative total numbers of galaxies, N_g, and random points, N_r, by dividing the summed pair weights DD, DR and RR for each separation bin by $N_g(N_g - 1)$, $N_g N_r$, and $N_r(N_r - 1)$, respectively.

The two-dimensional correlation function for our volume-limited sample of GAMA galaxies, along with the average correlation function from 26 mock samples, are shown in Fig. 2. Elongation of the clustering signal along the LOS ($r_\parallel$-axis) at small projected separations, $r_\perp \lesssim 5\,h^{-1}$ Mpc, and a compression of the LOS clustering

Figure 2. The two-dimensional correlation function $\xi(r_\perp, r_\parallel)$ for $M_r < -20$ volume-limited samples for (top) GAMA-II galaxies and (bottom) the average from 26 mock catalogues. To visually clarify departures from isotropy due to peculiar velocities, and to minimize aliasing effects when the Fourier transform is taken, the clustering signal is reflected about both axes. Following Li et al. (2006), contour levels increase by factors of 2 from $\xi = 0.1875$ to $\xi = 48$.

signal at larger separations are both clearly visible. For this plot, we have calculated $\xi(r_\perp, r_\parallel)$ in $1\,h^{-1}$ Mpc bins in both coordinates. We wish to determine the PVD measurement on the smallest possible scales, fully exploiting the high spectroscopic completeness of the GAMA survey. When estimating the PVD, we thus measure $\xi(r_\perp, r_\parallel)$ in logarithmically spaced bins in both directions, with $\log_{10}(r/\,h^{-1}$ Mpc) ranging from -2 to 2 in 20 bins.

Determination of the PVD also requires that the real-space correlation function $\xi_r(r)$ be known. We estimate $\xi_r(r)$ from the data via the projected correlation function, $w_p(r_\perp)$, which is obtained in the usual way by integrating the observed two-dimensional correlation function $\xi(r_\perp, r_\parallel)$ along the LOS direction $r_\parallel$:

$$w_p(r_\perp) = 2 \int_0^{r_{\parallel\mathrm{max}}} \xi(r_\perp, r_\parallel) \mathrm{d}r_\parallel. \qquad (3)$$

We use an upper integration limit of $r_{\parallel\mathrm{max}} = 40\,h^{-1}$ Mpc; see Appendix B for justification of this choice.

The real-space correlation function $\xi_r(r)$ may then be obtained by performing the inversion

$$\xi_r(r) = -\frac{1}{\pi} \int_r^\infty w_p(r_\perp) \left(r_\perp^2 - r^2\right)^{-1/2} \mathrm{d}r_\perp. \qquad (4)$$

This integral is evaluated by linearly interpolating between the binned $w_p(r_\perp)$ values (Saunders, Rowan-Robinson & Lawrence 1992); we use 20 logarithmically spaced bins from 0.01 to $100\,h^{-1}$ Mpc. Since this estimate of $\xi_r(r)$ can be be rather noisy, we also approximate $\xi_r(r)$ using a power-law fit to the projected correlation function $w_p(r_\perp)$ over the separation range $0.01\,h^{-1}$ Mpc $< r_\perp < 5\,h^{-1}$ Mpc. For a power-law fit, $\xi_r(r) = (r/r_0)^{-\gamma}$, equation (4) yields (Davis & Peebles 1983),

$$w_p(r_\perp) = A r_\perp^{1-\gamma}$$
$$A = r_0^\gamma \Gamma(1/2)\Gamma[(\gamma - 1)/2)]/ \Gamma(\gamma/2), \qquad (5)$$

where Γ is the standard gamma function.

4 MODELLING THE CORRELATION FUNCTION

Historically, two complementary approaches have been taken to model the two-dimensional galaxy correlation function in the presence of galaxy peculiar motions, the 'streaming' and 'dispersion' models. In this section, we briefly review these two models and then proceed to demonstrate that the peculiar velocity distribution function at small scales is reasonably well-fit by an exponential function for GAMA galaxies.

4.1 Streaming model

In the streaming model (e.g. Peebles 1980, 1993; Davis & Peebles 1983; Fisher 1995; Zehavi et al. 2002), $\xi(r_\perp, r_\parallel)$ is given by a convolution of the isotropic real-space correlation function $\xi_r(r)$ with the pairwise LOS velocity distribution $f(v_{12})$:

$$1 + \xi(r_\perp, r_\parallel) = H_0 \int_{-\infty}^\infty [1 + \xi_r(r)] \, f(v_{12}) \mathrm{d}y. \qquad (6)$$

Here, y is the true LOS separation of the galaxy pair, the total true separation is $r = \sqrt{r_\perp^2 + y^2}$, and $v_{12} = H_0(r_\parallel - y)$ is the relative LOS peculiar velocity.

The pairwise velocities are most often assumed to follow an exponential distribution:

$$f_e(v_{12}) = \frac{1}{\sqrt{2}\sigma_{12}(r_\perp)} \exp\left(-\frac{\sqrt{2}|v_{12} - \overline{v}_{12}|}{\sigma_{12}(r_\perp)}\right), \qquad (7)$$

or a Gaussian distribution

$$f_G(v_{12}) = \frac{1}{\sqrt{2\pi}\sigma_{12}(r_\perp)} \exp\left(-\frac{(v_{12} - \overline{v}_{12})^2}{2\sigma_{12}^2(r_\perp)}\right). \qquad (8)$$

The mean relative peculiar velocity of galaxies separated by a distance r (by symmetry directed along the separation vector $\boldsymbol{r}$) is given by $\overline{\boldsymbol{v}}_{12} = -H_0 g(r)\boldsymbol{r}$, and thus $\overline{v}_{12} = -H_0 g(r)y$ is the LOS component of this mean velocity. As discussed by Peebles (1993, p 478), one expects $g(r)$ to be close to unity on small scales where the peculiar velocity cancels out the Hubble flow within bound structures. At larger scales, $g(r)$ should tend to zero as uncorrelated galaxies move with the Hubble flow. In this work, we use the expression given by Juszkiewicz, Springel & Durrer (1999, equation 6, hereafter 'JSD model') for the mean radial pairwise velocity $\overline{v}_{12}(r)$.

The streaming model has been developed and improved by a number of authors, including Fisher (1995), Sheth (1996), Scoccimarro

(2004), Reid & White (2011), Bianchi, Chiesa & Guzzo (2015) and Uhlemann, Kopp & Haugg (2015), in order to find a more complete description of the velocity distribution function $f(v_{12})$. The main focus of these works has been to improve the model in the linear regime. In this work, we are focused on strongly non-linear scales, for which we show that assuming an exponential velocity distribution provides a good fit to simulations, provided that $\sigma_{12}(k)$ is allowed to vary with scale.

4.2 Dispersion model

Rather than assuming a model for the mean streaming velocity $\bar{v}_{12}(r)$, the dispersion model combines the Kaiser (1987) linear infall model with an assumed small-scale velocity distribution function. In Fourier space, the redshift space power spectrum $P_s(k, \mu)$ may be related to the real space power spectrum $P_r(k)$ by Peacock & Dodds 1994, Cole et al. 1995 and Jing & Borner 2001b[4]

$$P_s(k, \mu) = P_r(k)(1 + \beta\mu^2)^2 D(k\mu\sigma_{12}(k)), \tag{9}$$

where μ is the cosine of the angle between the wavevector $\boldsymbol{k}$ and the LOS. The factor $(1 + \beta\mu^2)^2$ is the Kaiser (1987) linear compression effect[5] and the factor D is the damping caused by random motions of galaxies. For an exponential form of the pairwise velocity distribution (equation 7), its Fourier transform D is a Lorentzian

$$D(k\mu\sigma_{12}(k)) = [1 + 0.5(k\mu\sigma_{12}(k))^2]^{-1}. \tag{10}$$

The Kaiser (1987) linear infall model has been translated from Fourier to configuration space by Hamilton (1992) to predict the shape of the two-dimensional correlation function $\xi'(r_\perp, r_\parallel)$ due to coherent infall:

$$\xi'(r_\perp, r_\parallel) = \xi_0(s)P_0(\mu) + \xi_2(s)P_2(\mu) + \xi_4(s)P_4(\mu), \tag{11}$$

where the $P_l(\mu)$ are Legendre polynomials and the harmonics of the correlation function are defined in Appendix C. One can then approximate the observed two-dimensional correlation function by convolving $\xi'(r_\perp, r_\parallel)$ with the peculiar velocity distribution, e.g. Hawkins et al. (2003),

$$\xi(r_\perp, r_\parallel) = \int_{-\infty}^{\infty} \xi'(r_\perp, r_\parallel - v_{12}/H_0)f(v)\mathrm{d}v, \tag{12}$$
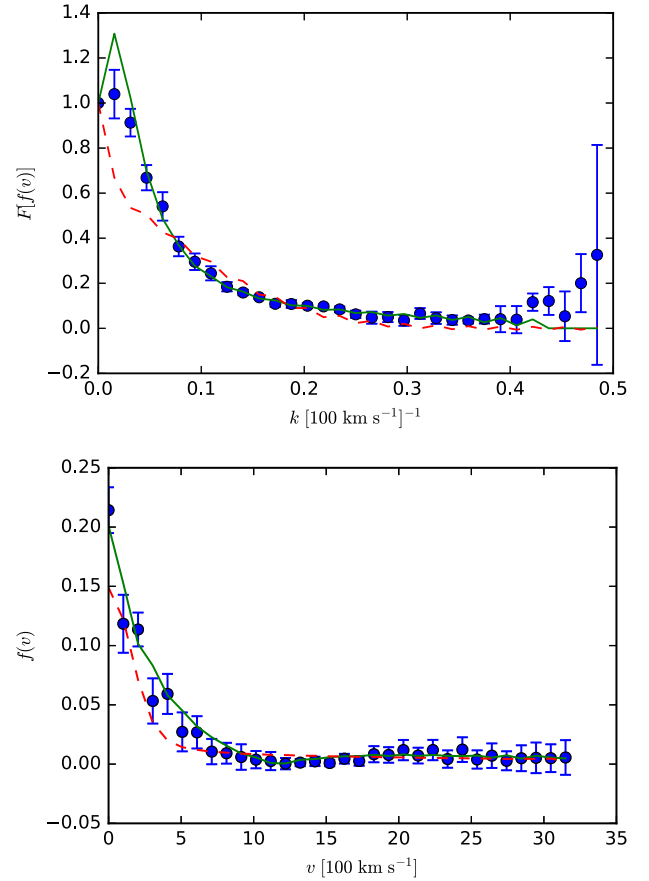
where $f(v_{12})$ is now assumed to be distributed around zero, and is thus given by equation (7) or (8) with $\bar{v}_{12} \equiv 0$.

4.3 Pairwise velocity distribution function

The previous work (e.g. Loveday et al. 1996; Landy et al. 1998; Hawkins et al. 2003) has found that the galaxy pairwise velocity distribution is better fit by an exponential than a Gaussian function. Sheth (1996) shows that an exponential distribution is expected on highly non-linear scales from Press–Schechter theory. We determine the pairwise velocity distribution for the GAMA-II data using the method of Landy et al. (1998), also used by Landy (2002) and Hawkins et al. (2003), which deconvolves the real-space correlation function from the peculiar velocity distribution.

Figure 3. The peculiar velocity distribution function (bottom) and its Fourier transform (top) for the GAMA V0 sample (symbols with error bars). The continuous green and red dashed lines show the best-fitting dispersion model predictions with exponential and Gaussian velocity distribution functions, respectively.

We take the 2D Fourier transform[6] of the $\xi(r_\perp, r_\parallel)$ grid measured out to 32 h^{-1} Mpc to give $\hat{\xi}(k_\perp, k_\parallel)$.[7] By the slicing-projection theorem (Landy et al. 1998), cuts of $\hat{\xi}(k_\perp, k_\parallel)$ along the $k_\perp$ and $k_\parallel$ axes, i.e. $\hat{\xi}(k_\perp, 0)$ and $\hat{\xi}(0, k_\parallel)$, are equivalent to the Fourier transforms of the real-space projections of $\xi(r_\perp, r_\parallel)$ on to the $r_\perp$ and $r_\parallel$ axes. The projection on to the $r_\perp$ axis is distortion free, whereas the projection on to the $r_\parallel$ axis gives the real-space correlation function convolved with the peculiar velocity distribution function. The ratio $\mathcal{F}[f(v_{12})](k) = \hat{\xi}(k_\perp = k, 0)/\hat{\xi}(0, k_\parallel = k)$ is thus the Fourier transform of the peculiar velocity distribution function; taking the inverse transform of this ratio yields $f(v_{12})$.

We fit the dispersion model to both the observations and mocks, with free parameters β and σ, by performing a χ^2 least-squares fit of the predicted to the measured $\mathcal{F}[f(v_{12})]$. We fit to $\mathcal{F}[f(v_{12})]$ rather than $f(v_{12})$ since the covariance matrix of $f(v_{12})$ estimates shows significant anticorrelations between odd and even-numbered bins. Both $\mathcal{F}[f(v_{12})]$ and the inferred $f(v_{12})$ for GAMA and mock volume-limited samples are shown in Figs 3 and 4, along with

---

[4] See Scoccimarro (2004) for an improved version of the dispersion model that allows for coupling between the velocity and density fields.

[5] The linear redshift distortion parameter $\beta = f(\Omega_m)/b$, where $f(\Omega_m) \approx \Omega_m^{0.6}$ is the dimensionless growth rate of structure in the linear regime and b is the galaxy bias parameter.

[6] We utilize the Numerical Python discrete Fourier transform package `numpy.fft`.

[7] The true power spectrum will only be obtained by taking the Fourier transform of the correlation function measured on all scales. We have verified that we get consistent results in this section when starting with $\xi(r_\perp, r_\parallel)$ measured out to 64 h^{-1} Mpc.
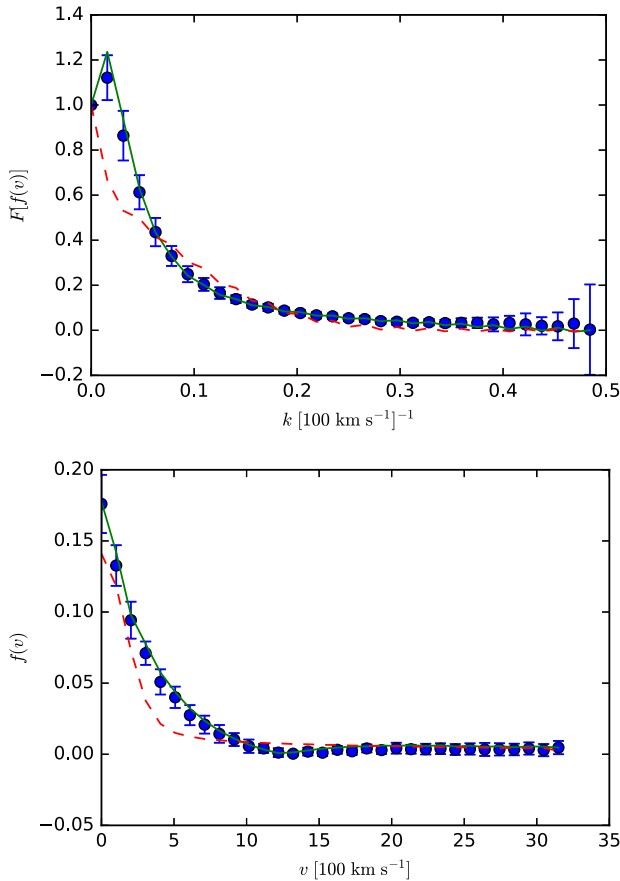
Figure 4. As Fig. 3 but from the average of 26 mock catalogues.

best-fitting predictions from dispersion models with exponential and Gaussian velocity distribution functions. The best-fitting parameters and χ^2 values are given in Table 2. It is clear that the exponential distribution function provides a much better fit to both the GAMA data and the mocks than the Gaussian distribution, which also gives unphysical, negative values for β. We therefore assume an exponential form for $f(v_{12})$ for the rest of this paper.

While this method is useful for determining the shape of the distribution function $f(v_{12})$, it is not ideal for estimating the values of β and the velocity dispersion σ_{12}, since it averages over a range of linear and non-linear separations. In fact, the value of β obtained for the mock V0 samples is completely inconsistent with the expected value of $\beta \approx 0.37$ (Section 2.4). The uncertainties quoted in Table 2 account only for scatter between realizations, and not for systematic errors due to inadequacies in the dispersion model when applied over a wide range of scales. In the following section, we obtain separation-dependent estimates of the velocity dispersion $\sigma_{12}(r_\perp)$ by fitting directly to the $\xi(r_\perp, r_\parallel)$ grid.

5 MOCK TESTS OF PVD ESTIMATORS

In this section, we test three methods for recovering the PVD from observational data, two based on the correlation function in redshift space, via the streaming and dispersion models, and one based on the dispersion model in Fourier space. All start with the 2d correlation function $\xi(r_\perp, r_\parallel)$, measured as described in Section 3, and are based on least-squares fitting of a model 2d correlation function or power spectrum to the measured one. The $\xi(r_\perp, r_\parallel)$ values are strongly correlated, and so one should in principle use the

full covariance matrix or its principal components (e.g. Norberg et al. 2009) in least-squares fitting. In practice, even when using mock catalogues, for which a covariance matrix may be reasonably well-determined, improvements over using just the diagonal elements are negligible, at best. With only nine jackknife samples for GAMA data, covariance matrix estimates are even more susceptible to noise. Therefore, all fitting to data is done using only diagonal elements of the covariance matrix. We show in Section 5.3 below that this introduces only a small bias in the inferred PVD using the dispersion model.

Before describing these clustering-based estimators of the PVD, we first discuss a direct measurement of the PVD from the mock catalogues, which will be used to test the veracity of the clustering-based estimates.

5.1 Direct mock-PVD measurement

Using the observed (z_{obs}) and cosmological (z_{cos}) redshifts provided in the mock galaxy catalogues, one can determine the LOS peculiar velocity (v_{pec}) for each galaxy using (Harrison 1974)

$$1 + v_{pec}/c = (1 + z_{obs})/(1 + z_{cos}). \tag{13}$$

We then define the relative LOS velocity for a pair of galaxies as $v_{12} = v_{pec, 2} - v_{pec, 1}$, where galaxy 1 is the closer of the pair, so that v_{12} is negative for galaxies that are approaching each other. Note that this formula is only accurate for galaxy pairs at small angular separation, and so we limit our measurements to pairs of galaxies separated by less than 12° (the RA extent of each GAMA region).

The LOS pairwise velocity distributions for mock galaxy pairs in four representative bins of projected separation, including all pairs along the line-of-sight direction up to $r_\parallel = 50\,h^{-1}\,$Mpc, are shown in Fig. 5. Visually, the distributions are reasonably well-fit by exponential functions for galaxy pairs at projected separation $r_\perp \lesssim 1\,h^{-1}\,$Mpc (e.g. top two panels), even though the reduced χ^2 values formally rule out an exponential fit (the standard error from the scatter between mock realizations is tiny). At larger separations, a growing skewness in the distributions towards negative velocities,[8] and decreasing random errors, result in poorer fits. It is clear that a Gaussian grossly underfits the tails of the distribution at all separations.

For pairs of galaxies in logarithmically spaced separation bins ($r_\perp, r_\parallel$) in redshift space, we calculate the mean and standard deviation of the pairwise LOS velocity distribution, $\overline{v}_{12}$ and σ_{12}, respectively, as well as the maximum-likelihood velocity dispersion σ_{12}^{exp} for an exponential distribution (equation 7), namely

$$\sigma_{12}^{exp} = \frac{\sqrt{2}}{N} \sum_{i=1}^{N} |v_{12,i} - \overline{v}_{12}|, \tag{14}$$
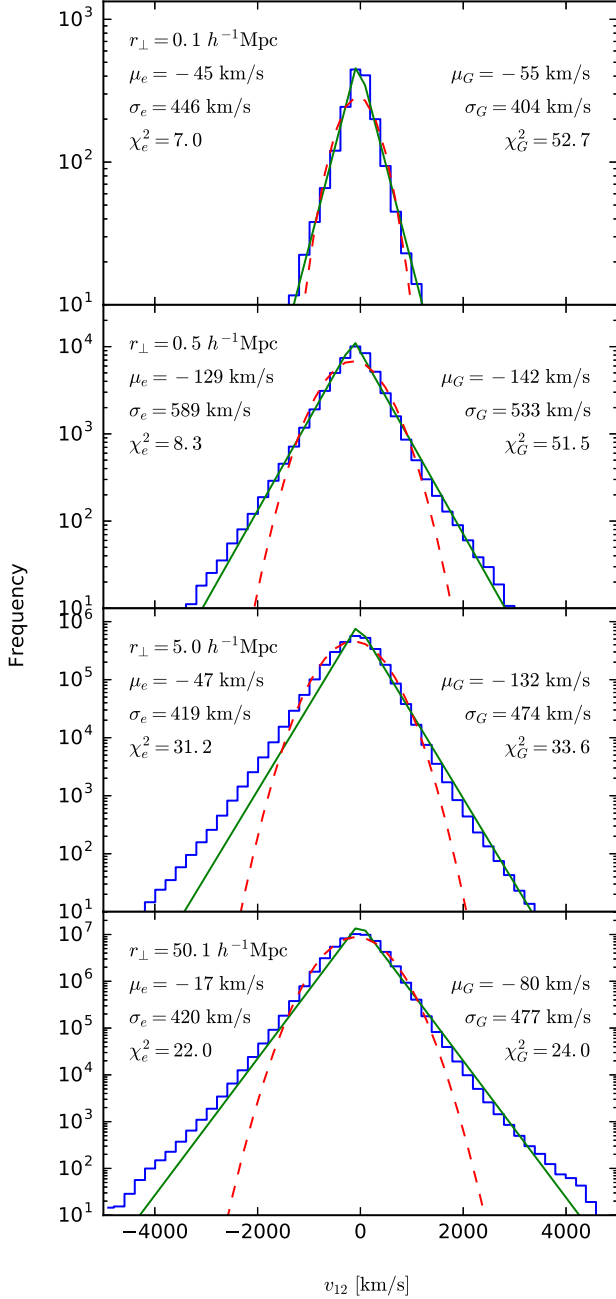
where the sum is carried out over all N galaxy pairs in each separation bin.

In Fig. 6, we show the mean and exponential dispersion of the mock LOS pairwise velocities in bins of two-dimensional redshift-space separation. It is interesting to see that the largest (negative) mean velocities and dispersions occur at very different separation bins. The most negative mean velocities of $\overline{v}_{12} \lesssim -300\,$km s^{-1}
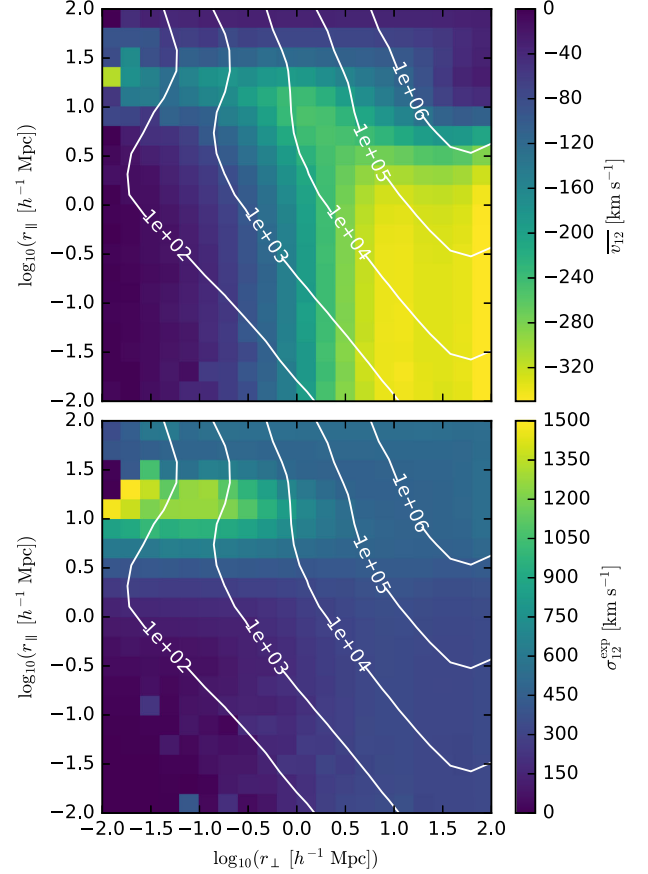
---

[8] This skewness in the pairwise velocity distribution has previously been reported from simulations by Juszkiewicz, Fisher & Szapudi (1998) and Magira, Jing & Suto (2000). See Bianchi, Chiesa & Guzzo (2015) and Bianchi, Percival & Bel (2016) for a bivariate Gaussian description for the pairwise velocity distribution function that can account for this asymmetry.

Table 2. Fits of β infall parameter and velocity dispersion σ_{12} (in km s^{-1}) to the Fourier transformed velocity distribution function for both the GAMA V0 sample and the mean of the 26 mock V0 samples. For all fits there are 29 degrees of freedom.

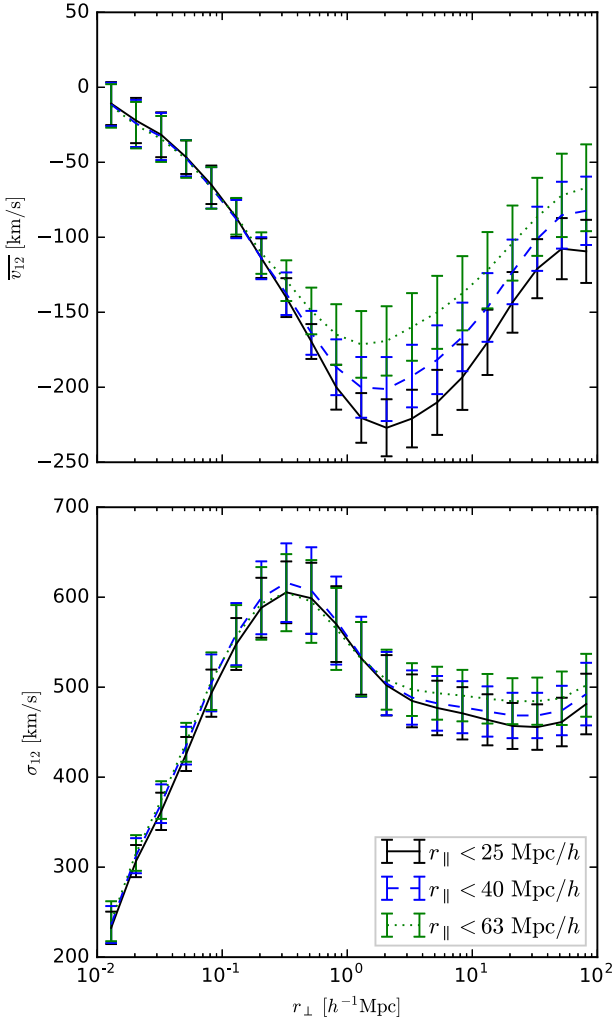|	GAMA			Mocks		
Model	β	σ_{12}	χ^2	β	σ_{12}	χ^2
Exponential	0.75 ± 0.03	676 ± 34	32	0.68 ± 0.05	690 ± 71	5
Gaussian	-0.88 ± 0.08	106 ± 12	178	-0.92 ± 0.04	111 ± 10	112

Figure 5. LOS relative velocity distributions for mock galaxy pairs (stepped histograms), exponential fits (continuous lines) and Gaussian fits (dashed lines) in four bins of projected separation as labelled. We include all pairs along the line of sight direction up to $r_\parallel = 50\,h^{-1}$ Mpc. Fit parameters and reduced χ^2 values are shown for the exponential fits on the left and for Gaussian fits on the right.

Figure 6. Mean (top) and exponential dispersion (bottom) of the mock LOS pairwise velocities, in logarithmic bins of redshift space separation. Contour lines from left to right connect bins containing 10^2, 10^3, 10^4, 10^5 and 10^6 galaxy pairs.

are seen at projected separation $r_\perp \gtrsim 3\,h^{-1}$ Mpc and LOS separation $r_\parallel \lesssim 3\,h^{-1}$ Mpc. The highest velocity dispersions, of up to $\sigma_{12}^{\rm exp} \approx 1500$ km s^{-1}, are seen at $r_\perp \lesssim 1\,h^{-1}$ Mpc and $10 \lesssim r_\parallel \lesssim 30\,h^{-1}$ Mpc. The PVD is uniformly low, $\sigma_{12}^{\rm exp} \lesssim 300$ km s^{-1}, at LOS separations $r_\parallel \lesssim 5\,h^{-1}$ Mpc regardless of projected separation $r_\perp$.

Values of $\bar{v}_{12}(r_\perp)$ and $\sigma_{12}^{\rm exp}(r_\perp)$ as a function of projected separation $r_\perp$ alone are obtained by averaging over $r_\parallel$ separation bins, weighting by the number of galaxy pairs per bin. It is clear that most of the contribution to the velocity dispersion $\sigma_{12}^{\rm exp}(r_\perp)$ will come from LOS separations $5 \lesssim r_\parallel \lesssim 30\,h^{-1}$ Mpc. The estimated dispersion is insensitive to the upper limit of LOS separation beyond $r_\parallel \approx 30\,h^{-1}$ Mpc due to the modest drop in $\sigma_{12}^{\rm exp}$ values at larger $r_\parallel$. The estimated mean velocity $\bar{v}_{12}(r_\perp)$ *is* sensitive to the limiting $r_\parallel$ due to the steady decline in $|\bar{v}_{12}|$ beyond $r_\parallel \gtrsim 30\,h^{-1}$ Mpc, so that the amplitude of $\bar{v}_{12}(r_\perp)$ decreases with increasing $r_{\parallel\,{\rm max}}$. Since galaxies with LOS separation $r_\parallel \gtrsim 40\,h^{-1}$ Mpc ($\Delta v \gtrsim 4000$ km s^{-1}) are
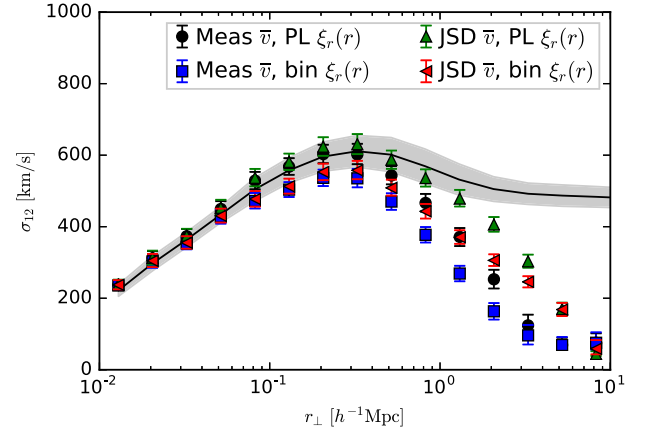
Figure 7. LOS mean pairwise velocity $\overline{v}_{12}$ (upper panel), and velocity dispersion σ_{12} (lower panel) for pairs of mock galaxies as a function of projected separation. The different line styles and colours represent different upper limits to projected separation $r_\parallel$ as indicated in the lower panel.

unlikely to be correlated, we impose an upper limit of $r_\parallel = 40\,h^{-1}$ Mpc when calculating $\overline{v}_{12}(r_\perp)$ and $\sigma_{12}^{\rm exp}(r_\perp)$.

Note that it is unlikely that the mock catalogues have sufficient resolution to reliably predict galaxy dynamics on scales below about $0.1\,h^{-1}$ Mpc. Nevertheless, by comparing clustering-inferred estimates of the PVD with those obtained directly from the peculiar velocity information, we can still use the mocks to test our methods down to scales $r_\perp = 0.01\,h^{-1}$ Mpc.

Maximum-likelihood estimates of mean pairwise velocity and exponential velocity dispersion are shown in Fig. 7 as a function of projected separation $r_\perp$, including pairs with LOS separation up to three different values of $r_\parallel$ as indicated in the lower panel. We see net LOS infall between pairs of galaxies on all scales, with maximum infall of $\overline{v}_{12}(r_\perp) \approx -200\,{\rm km\,s^{-1}}$ at separation $r_\perp \approx 2\,h^{-1}$ Mpc with $r_\parallel < 40\,h^{-1}$ Mpc. Exponential velocity dispersion rises from $\sigma_{12}^{\rm exp}(r = 0.01\,h^{-1}\,{\rm Mpc}) \approx 200\,{\rm km\,s^{-1}}$, peaking at $\sigma_{12}^{\rm exp}(r \approx 0.4\,h^{-1}\,{\rm Mpc}) \approx 600\,{\rm km\,s^{-1}}$ and tending to $\sigma_{12}^{\rm exp}(r \approx 100\,h^{-1}\,{\rm Mpc}) \approx 500\,{\rm km\,s^{-1}}$ on large scales. Note that the velocity dispersion estimates are insensitive to the upper limit of projected separation.

Figure 8. Pairwise LOS velocity dispersion estimates from the mock galaxy V0 samples. The continuous line and shaded region show the direct estimate of $\sigma_{12}(r_\perp)$ and its standard deviation reproduced from Fig. 7. Symbols show PVD estimates recovered by fitting the streaming model (Section 5.2) to the two-dimensional correlation function. Black circles and blue squares show results using the measured $\overline{v}_{12}(r)$ and power-law and binned measurements of $\xi_{\rm r}(r)$, respectively. Green and red triangles show results using the JSD model $\overline{v}_{12}(r)$ and power-law and binned measurements of $\xi_{\rm r}(r)$, respectively.

Having made a direct measurement of the PVD from the mock catalogues, we can now investigate PVD estimates based on the anisotropy of redshift-space clustering.
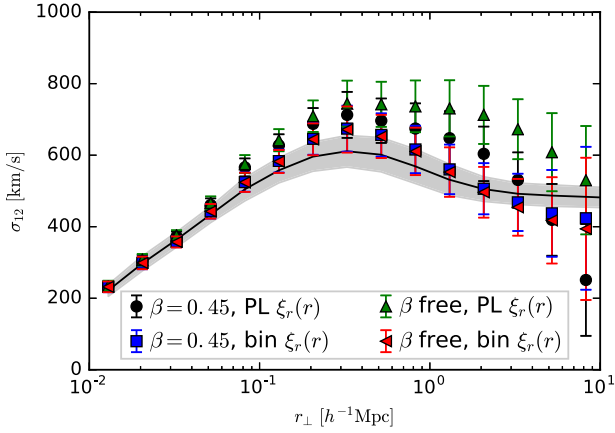
5.2 Streaming model

We find the velocity dispersion $\sigma_{12}(r_\perp)$ in bins of projected separation $r_\perp$ by least-squares fitting of the observed two-dimensional correlation function $\xi(r_\perp, r_\parallel)$ with the prediction from equation (6), using LOS bins $r_\parallel < 40\,h^{-1}$ Mpc. We test this estimator for the PVD using the volume-limited mock catalogues in Fig. 8. We compare results obtained using power-law and binned estimates of $\xi_{\rm r}(r)$, as well as both directly measured and the JSD model for mean-streaming velocities $\overline{v}_{12}(r)$. All estimates are consistent with the directly determined PVD on small scales, $r_\perp \lesssim 0.3\,h^{-1}$ Mpc; all tend to underestimate the PVD on larger scales. Of the four variants of this estimator, that using the JSD model for $\overline{v}_{12}$ along with a power-law fit for $\xi_{\rm r}(r)$, performs better than the others, providing reliable estimates of the PVD to $r_\perp \lesssim 1\,h^{-1}$ Mpc.
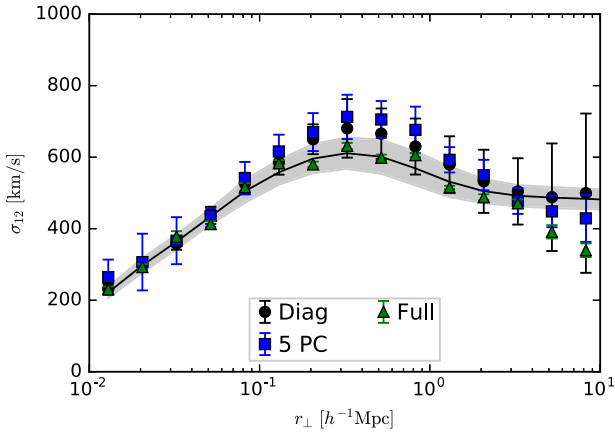
5.3 Dispersion model in configuration space

We find the velocity dispersion $\sigma_{12}(r_\perp)$ in bins of projected separation $r_\perp$ by least-squares fitting of the observed two-dimensional correlation function $\xi(r_\perp, r_\parallel)$ with the prediction from equation (12), using LOS bins $r_\parallel < 40\,h^{-1}$ Mpc. We test this estimator for the PVD using the volume-limited mock catalogues in Fig. 9. This plot shows results using both power-law fits and binned measurements of the real-space correlation function $\xi_{\rm r}(r)$, and also with β fixed at $\beta = 0.45$ or allowed to vary as a free parameter. It is clear that the binned estimates of $\xi_{\rm r}(r)$ (blue squares and red triangles for fixed and free β, respectively) give a more reliable measure of the PVD over a wider range of scales than a single power-law fit to $w_{\rm p}(r_\perp)$ (black circles and green triangles). The former measurements lie within $\approx 1\sigma$ of the directly determined PVD on all scales from 0.01 to 10 h^{-1} Mpc.

Fig. 10 explores the effects of using the full covariance matrix of the correlation function measurements $\xi(r_\perp, r_\parallel)$, just the diagonal

Figure 9. As Fig. 8 but showing PVD estimates recovered by fitting the dispersion model (Section 5.3) to the two-dimensional correlation function. Black circles show the results of using a power-law fit to $w_p(r_\perp)$ to predict $\xi_r(r)$, blue squares use a numerical inversion of the binned $w_p(r_\perp)$ measurements to predict $\xi_r(r)$. Both of these measurements assume a fixed value of $\beta = 0.45$. Allowing β to vary as a free parameter, the power-law $\xi_r(r)$ favours $\beta = 0.66$ (green triangles); the binned $\xi_r(r)$ favours $\beta = 0.43$ (red triangles).

Figure 10. Dispersion model estimates of the PVD using the full covariance matrix of $\xi(r_\perp, r_\parallel)$ (green triangles), the diagonal components only (black circles), or the first five principal components (blue squares). We use binned $\xi_r(r)$ measurements and hold β fixed at $\beta = 0.5$.
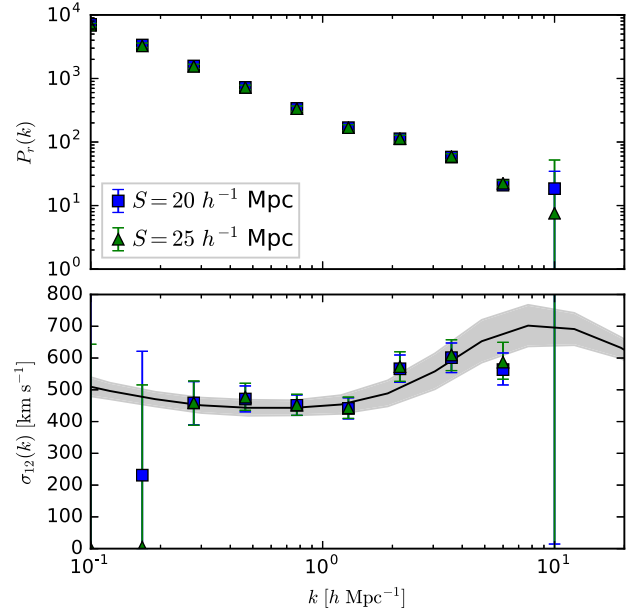
components, or the first five principal components, when fitting the dispersion model. While we see that using the full covariance matrix improves the estimates on scales $r_\parallel \lesssim 1\,h^{-1}$ Mpc, they are worsened on larger scales. The full covariance matrix estimates for the GAMA data will be nosier than those for the 26 mock realizations, and so for our main results we use only the diagonal elements.

5.4 Dispersion model in Fourier space

We determine the redshift space power spectrum $P_s(k, \mu)$ from the two-dimensional correlation function $\xi(r_\perp, r_\parallel)$ using the method of Jing & Borner (2004):

$$P_s(k, \mu) = 2\pi \sum_{i,j} \Delta r_{\parallel i}^2 \Delta \ln r_{\perp j} \xi(r_{\perp j}, r_{\parallel i}) \cos(k_\parallel r_{\parallel i})$$
$$\times J_0(k_\perp r_{\perp j}) W_g(r_{\perp j}, r_{\parallel i}),$$

where J_0 is the zeroth-order Bessel function. Following Li et al. (2006), $r_{\parallel i}$ runs from -40 to $40\,h^{-1}$ Mpc with $\Delta r_{\parallel i} = 1\,h^{-1}$ Mpc

Figure 11. Real-space power spectrum $P_r(k)$ (top panel) and pairwise velocity dispersion $\sigma_{12}(k)$ (bottom panel) estimated from the mock catalogues using the methods described in Section 5.4. The continuous line and shaded region in the lower panel show the direct estimate of the real-space exponential velocity dispersion $\sigma_{12}^{\exp}(r)$ and its standard deviation reproduced from Fig. 7, assuming that $k = 2\pi/r$. Blue squares and green triangles, respectively, denote smoothing scales of $S = 20, 25\,h^{-1}$ Mpc in equation (15).

and $r_{\perp j}$ runs from 0.1 to 50 h^{-1} Mpc with $\Delta \ln r_{\perp j} = 0.23$. W_g is a Gaussian window function used to down-weight noisy $\xi(r_\perp, r_\parallel)$ measurements at large scales:

$$W_g(r_\perp, r_\parallel) = \exp\left(-\frac{r_\perp^2 + r_\parallel^2}{2S^2}\right), \qquad (15)$$
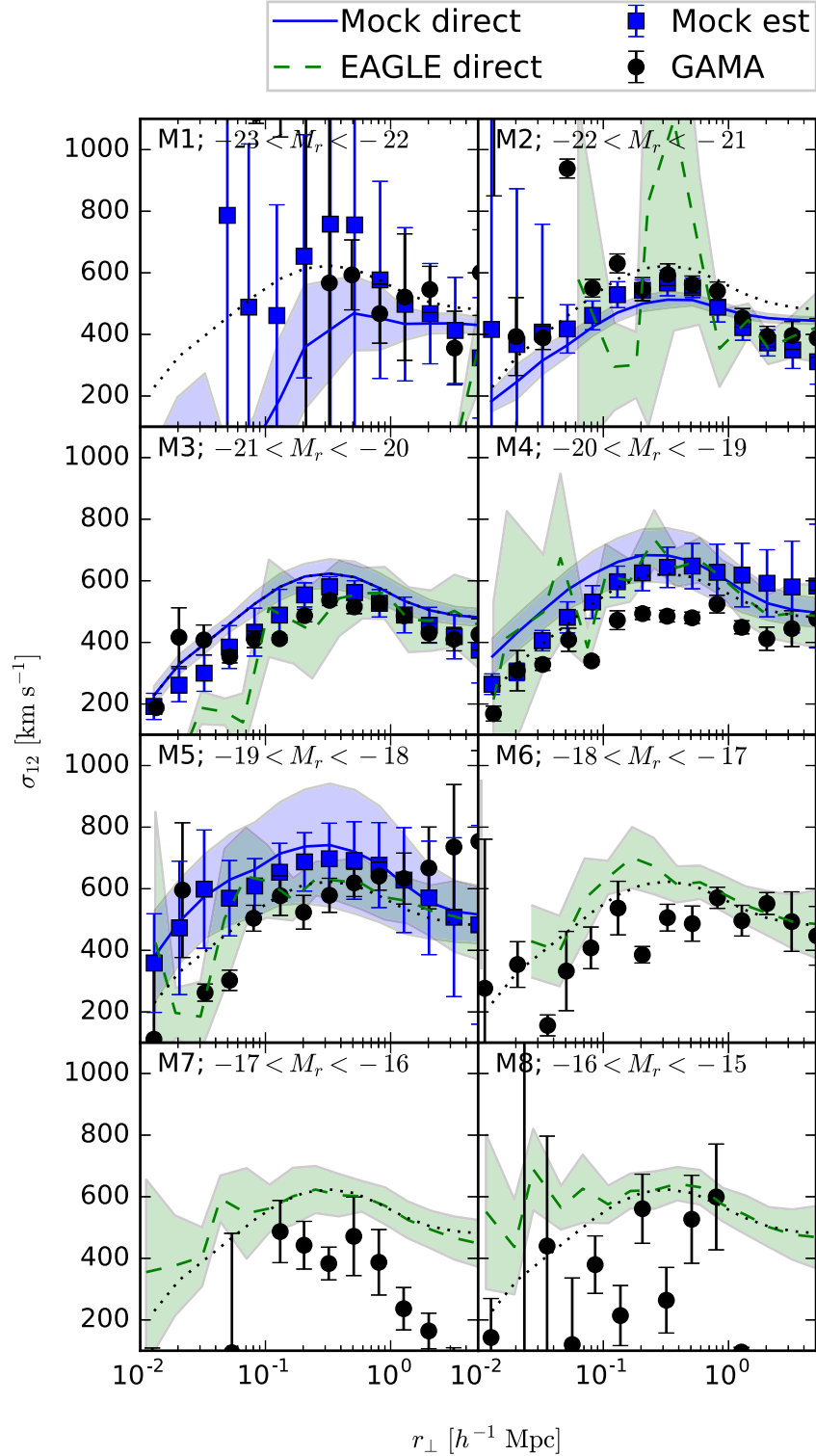
with smoothing scale $S = 20$ or $25\,h^{-1}$ Mpc.

As advised by Jing & Borner (2001a), we reduce the effects of finite bin sizes in $r_\parallel$ and $r_\perp$ by dividing each $r_\parallel$ and $\ln r_\perp$ bin into N sub-bins and interpolate $\xi(r_\parallel, r_\perp)$ at each sub-bin using a bilinear cubic spline. We have found that $N = 21$ sub-bins is sufficient to obtain reliable $P_s(k, \mu)$ measurements on small scales (large k values).

In Fig. 11, we show the real-space power spectrum $P_r(k)$ and pairwise velocity dispersion $\sigma_{12}(k)$ estimated from the mock catalogues by fitting the model $P_s(k, \mu)$ (equation 9) to the observed one, assuming a fixed value of $\beta = 0.45$. The $2 \times n_k$-parameters, where n_k is the number of bins in which $P_r(k)$ and $\sigma_{12}(k)$ are estimated, and the covariances between the parameters, are determined using the EMCEE (Foreman-Mackey et al. 2013) Markov Chain Monte Carlo code. Both power spectrum and velocity dispersion measurements become very noisy at small scales, $k \gtrsim 8\,h$ Mpc^{-1} or $r \lesssim 0.6\,h^{-1}$ Mpc. At larger scales, $k \lesssim 8\,h$ Mpc^{-1}, the PVD estimated in Fourier is in very good agreement with the direct estimate, particularly with a smoothing length of $25\,h^{-1}$ Mpc.

5.5 Summary of tests

From these tests using mock catalogues, we conclude that the configuration space dispersion model provides the most reliable

Figure 12. Pairwise velocity dispersions with projected separation $r_\perp$ in bins of absolute magnitude as defined in Table 1. Blue and green lines show direct estimates from the GALFORM mocks and EAGLE simulation, respectively, with the 1σ error band shaded in both cases. Blue squares and black circles show dispersion model estimates from the mocks and GAMA galaxies, respectively. To aid visual comparison, the dotted line reproduces the direct mock estimate for the M3 sample in the other panels. The mock error bars show the standard deviation from 26 realizations; the GAMA error bars are determined from jackknife sampling. The mock error bars are slightly larger than the GAMA ones, accounting as they do more fully for sample variance.

estimate of the PVD on scales $(0.01\,h^{-1}\,\mathrm{Mpc} \lesssim r_\perp \lesssim 10\,h^{-1}\,\mathrm{Mpc})$. The Fourier-space dispersion model provides reliable estimates on larger scales $(0.6\,h^{-1}\,\mathrm{Mpc} \lesssim r_\perp \gtrsim 30\,h^{-1}\,\mathrm{Mpc})$. We show results using both of these methods in the following section.

6 RESULTS AND DISCUSSION

In Fig. 12, we show the PVD σ_{12} as a function of projected separation in bins of absolute magnitude for both GAMA and mock

galaxies. In each panel, for luminosity bins M1–M5, one should first compare the direct (blue line) and dispersion model (blue squares) estimates from the mocks. If these are in good agreement, then the GAMA dispersion-model results are likely to be reliable. The space density of galaxies in bin M1 is too low for a reliable estimate of the PVD on small scales, but the estimates converge for separations $r_\perp \gtrsim 1\,h^{-1}$ Mpc. For the remaining luminosity bins, M2–M5, agreement between direct and dispersion-model estimates of the mock PVDs is excellent on all scales measured.
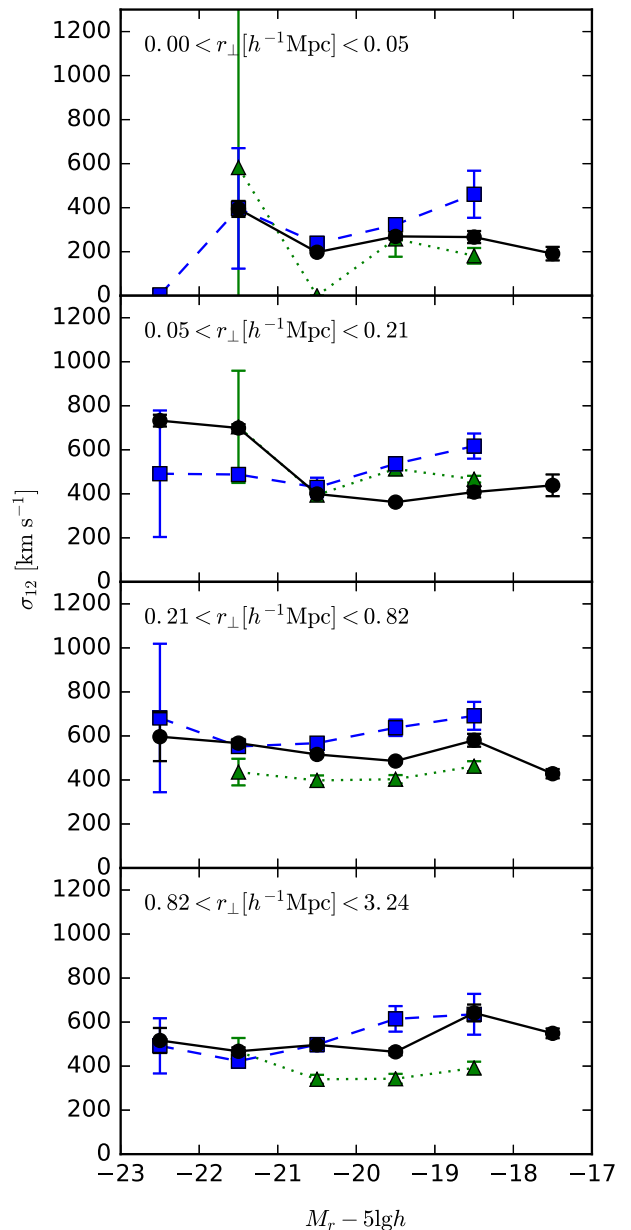
Comparing GAMA and mock PVDs, for luminous galaxies, bins M1–M3, the amplitudes are consistent, and both peak at $r_\perp \approx 0.3\,h^{-1}$ Mpc. For fainter galaxies, bins M4 and M5, the mock PVDs are systematically higher than the GAMA PVDs. This is particularly noticeable for bin M4, where the GAMA estimates are unusually low. Since the large-scale GAMA PVD increases again in lower-luminosity bins, M5 and M6, this is most likely a sampling fluctuation, perhaps due to the significant underdensity in the GAMA redshift distribution around $z \approx 0.2$–0.26, a region from which many of the galaxies in bin M4 lie (see figs 4 and 5 of Farrow et al. 2015).

Since the GALFORM mock catalogues are reliable at only relatively bright magnitudes ($M_r \lesssim -17$ mag), we also compare our GAMA PVD estimates with those from EAGLE hydrodynamical simulation RefL0100N1504 (Crain et al. 2015; Schaye et al. 2015; McAlpine et al. 2016). Placing the observer at the origin of the $z = 0.1$ data cube, we use the Cartesian velocities of each subhalo to calculate the line-of-sight peculiar velocity of each galaxy, and hence the PVD, as a function of projected separation. Uncertainties are estimated by subdividing the simulation cube into eight sub-cubes and calculating jackknife errors. We have verified that EAGLE r-band absolute magnitudes are consistent with GAMA: the luminosity functions agree extremely well over the magnitude range $-22 < M_r < -15$. We therefore use the same absolute magnitude limits when comparing EAGLE with GAMA. Note that Artale et al. (2017) have recently compared small-scale galaxy clustering in EAGLE with GAMA, and find very good agreement.

EAGLE simulation results, shown in Fig. 12 as a green line, are noisy for luminous galaxies due to the limited volume probed (10^6 Mpc^3 for $h = 0.6777$). For moderate luminosities (bins M3–M5), the agreement with GALFORM is good. The GAMA PVD is also consistent with EAGLE for bin M6, but falls below the EAGLE prediction for the two faintest bins, M7 and M8. The GAMA jackknife errors likely underestimate the uncertainties in these very small volume samples, and so this is not necessarily indicating a discrepancy with EAGLE at low luminosities.

To show the PVD dependence on luminosity more clearly, in Fig. 13 we show the PVD σ_{12} as a function of absolute magnitude in broad bins of projected separation. To do this, we determine the average PVD for four sets of three adjacent separation bins, with separation limits as given in the figure legend. When averaging, we weight each bin by its inverse-variance, and the variance on the average is determined in the usual way as the reciprocal of the sum of inverse-variances.
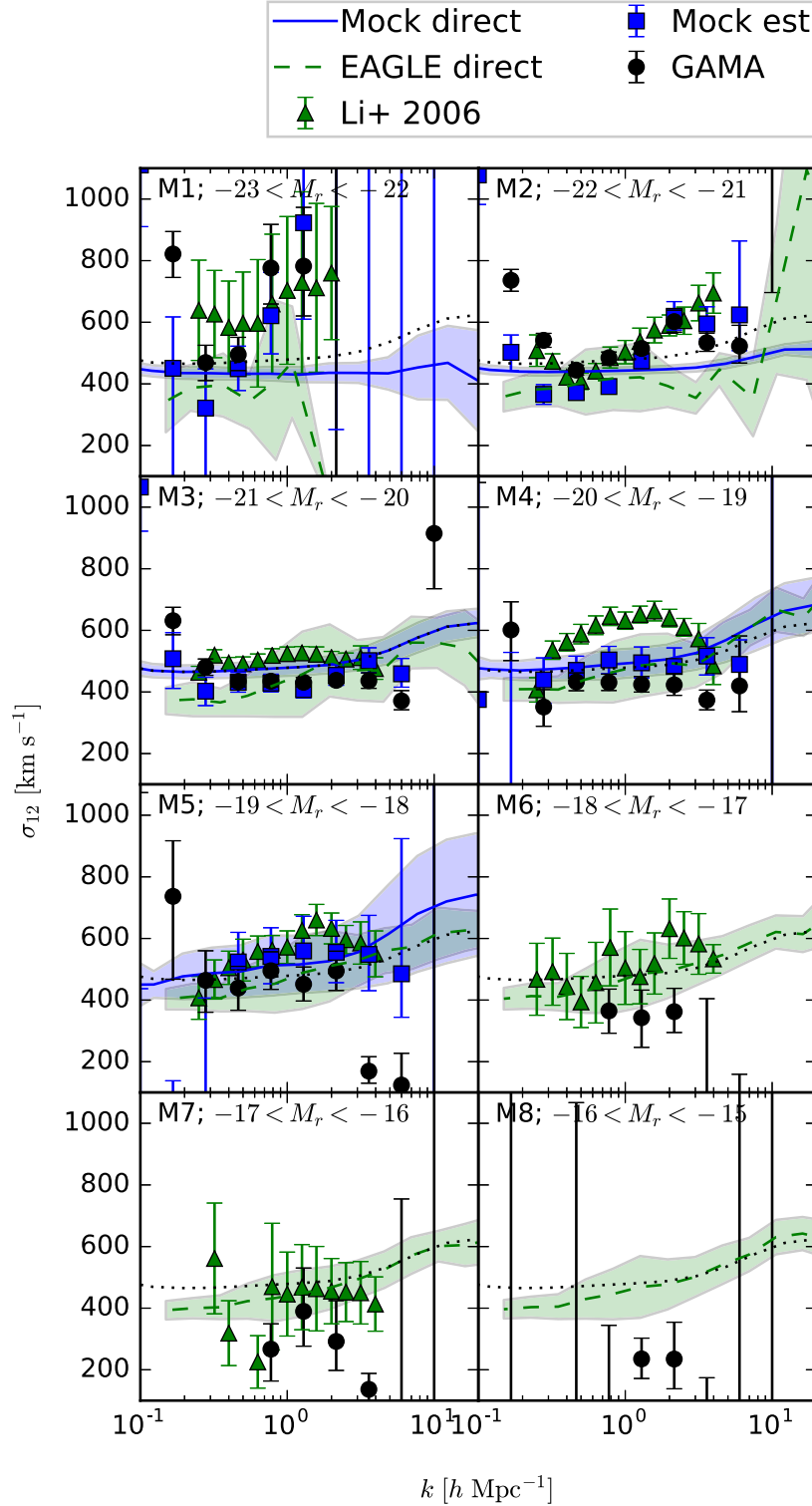
For small scales, $r_\perp \lesssim 1\,h^{-1}$ Mpc, corresponding to the top three panels, the PVD for GAMA galaxies tends to decline near-monotonically from bright to faint luminosities. The mock PVD is much flatter, possibly even showing a small increase to fainter luminosities. Thus, the mocks do a good job at matching the observed PVD for luminous galaxies, but overpredict the PVD for fainter objects. The same result was found by Li et al. (2007) when comparing two previous Millennium-based semi-analytic models (Kang et al. 2005; Croton et al. 2006) with SDSS PVD measure-

Figure 13. Pairwise velocity dispersion for GAMA galaxies (black circles connected by continuous lines) and mocks (blue squares connected by dashed lines) as a function of absolute magnitude in bins of projected separation $r_\perp$ as labelled. Green triangles connected by dotted lines show the PVD for galaxies selected from a volume-limited sample with $M_r < -18$ mag.

ments. Li et al. (2007) show that the mocks most likely place too many faint galaxies in massive haloes. This problem thus appears to persist in more recent semi-analytic models. This interpretation is reinforced by the fact that the same mock catalogue significantly overpredicts the small-scale projected correlation function of faint ($M_r > -18$ mag) galaxies (Farrow et al. 2015, fig. 11).

One should, however, be aware that the faintest galaxies can only be seen in the very nearby Universe. Thus, if the local volume is underdense, as has been claimed by several authors (e.g. Busswell et al. 2004; Keenan, Barger & Cowie 2013; Whitbourn & Shanks 2016), a paucity of local, large structures might explain the low observed PVD and projected clustering for the faintest galaxies. In order to address this concern, we have defined a second,

Figure 14. Pairwise velocity dispersions with wavenumber k in bins of absolute magnitude. Blue and green lines show direct estimates from the GALFORM mocks and EAGLE simulation, respectively, with the 1σ error band shaded in both cases. Blue squares and black circles show Fourier-space estimates from the mocks and GAMA galaxies, respectively. Green triangles show estimates from SDSS (Li et al. 2006). To aid visual comparison, the dotted line reproduces the direct mock estimate for the M3 sample in the other panels.

fainter, volume-limited sample from GAMA with $^{0.1}M_r < -18$ mag and $z < 0.116$. We then extract subsamples in bins of absolute magnitude $[-22, -21]$, $[-21, -20]$, $[-20, -19]$, $[-19, -18]$. The galaxies in these absolute magnitude bins are visible throughout the

volume and hence will not suffer from sampling fluctuations due to Malmquist bias. We show the PVDs from this volume-limited sample as green triangles in Fig. 13. While the trend with luminosity is less clear than for the full GAMA sample, the results are

broadly consistent. Unfortunately, one cannot extend this analysis to the full luminosity range plotted due to the tiny volume within which fainter galaxies can be seen. Note that forming a (separate) volume-limited sample for each luminosity bin would not alleviate sampling fluctuations.

In Fig. 14, we show the Fourier-based PVD estimate as a function of wavenumber k. From comparison with the direct mock estimates, we conclude that these Fourier-based PVD estimates should be reliable for moderate luminosity galaxies (bins M2–M5, $-22 \lesssim M_r \lesssim -18$) over the range of scales $0.2 \lesssim k \lesssim 5\,h\,\mathrm{Mpc}^{-1}$. We also show comparison results from Li et al. (2006). Given the uncertainties, our results are broadly consistent with those of Li et al. where we overlap, although we do measure systematically lower PVD than Li et al. for the M4 ($-20 < M_r < -19$ mag) bin.

In future, we plan to investigate the dependence of the PVD on location within the cosmic web, on stellar mass and on redshift. We also plan to investigate improvements to the mock catalogues to better match the luminosity-dependence of the observed galaxy PVD, along with other observational constraints. In the longer term, it is hoped that such measurements may be instrumental in ruling out certain models of modified gravity.

7 CONCLUSIONS

We have presented measurements of the PVD for luminosity-selected samples of galaxies from the GAMA equatorial regions, using mock catalogues to check our estimators. GAMA's relatively deep flux limit, $r < 19.8$, and high redshift success rate, >98 per cent, have enabled us to measure the PVD down to a factor of 10 smaller in projected separation than was possible using SDSS data (Li et al. 2007). Our findings can be summarized as follows.

(i) In agreement with previous work (e.g. Hawkins et al. 2003), we find that the form of the pairwise velocity distribution is much better fit by an exponential than a Gaussian function.

(ii) The dispersion model can make reliable predictions of the PVD in configuration space for galaxy pairs with projected separation 0.01–10 h^{-1} Mpc, thus allowing detailed tests of galaxy formation models and hydrodynamical simulations.

(iii) In Fourier space, one can reliably measure the PVD of GAMA galaxies for wave numbers in the range 0.2–8 $h\,\mathrm{Mpc}^{-1}$. This is similar to the range of scales probed by Li et al. (2007) using SDSS data; thus the Fourier method employed here does not enable us to exploit the small-scale fidelity of the GAMA data as well as configuration-space methods.

(iv) For most luminosity bins, the PVD peaks at $\sigma_{12} \approx 600\,\mathrm{km\,s}^{-1}$ at projected separations $r_\perp \approx 0.3\,h^{-1}$ Mpc, although some fainter bins show a monotonic increase in σ_{12} with separation.

(v) On small scales, $r_\perp \lesssim 1\,h^{-1}$ Mpc, the measured PVD for GAMA galaxies declines slightly from $\approx 600\,\mathrm{km\,s}^{-1}$ at high luminosities to $\approx 400\,\mathrm{km\,s}^{-1}$ at low luminosities. This trend is not seen at larger scales (0.8–3.3 h^{-1} Mpc).

(vi) While the GALFORM mocks analysed here give a similar-amplitude PVD as the GAMA galaxies, they show very little trend with luminosity: if anything, they predict a slightly increasing PVD with decreasing luminosity for L^* and fainter galaxies. Thus, the mocks do a good job at matching the observed PVD for luminous galaxies, but overpredict the PVD for fainter objects.
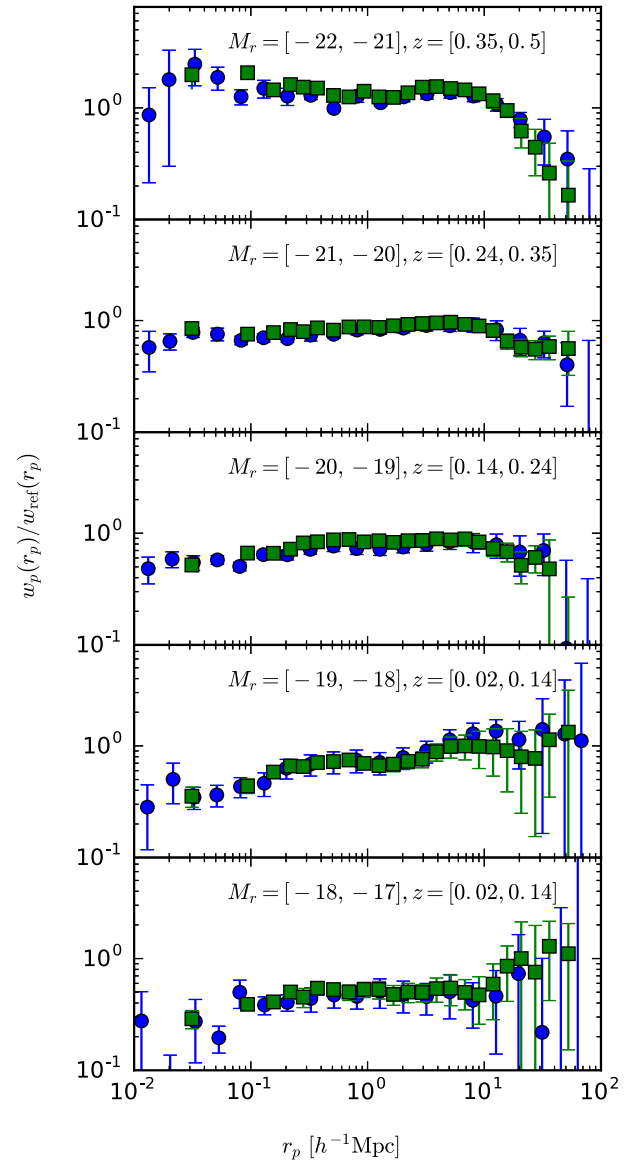
ACKNOWLEDGEMENTS

REFERENCES

Abazajian K. N. et al., 2009, ApJS, 182, 543
Artale M. C. et al., 2017, MNRAS, 470, 1771
Baldry I. K. et al., 2010, MNRAS, 404, 86
Baldry I. K. et al., 2012, MNRAS, 421, 621
Baldry I. K. et al., 2014, MNRAS, 441, 2440
Bartlett J. G., Blanchard A., 1996, A&A, 307, 1
Bean A. J., Ellis R. S., Shanks T., Efstathiou G., Peterson B. A., 1983, MNRAS, 205, 605
Berlind A. A. et al., 2003, ApJ, 593, 1
Bianchi D., Chiesa M., Guzzo L., 2015, MNRAS, 446, 75
Bianchi D., Percival W. J., Bel J., 2016, MNRAS, 463, 3783
Bibiano A., Croton D. J., 2017, MNRAS, 467, 1386
Blake C. et al., 2013, MNRAS, 436, 3089
Blanton M. R., Roweis S., 2007, AJ, 133, 734
Busswell G. S., Shanks T. W. J. Frith P. J. O., Metcalfe N., Fong R., 2004, MNRAS, 354, 991
Cabré A., Gaztañaga E., 2009, MNRAS, 396, 1119
Cole S., 2011, MNRAS, 416, 739
Cole S., Fisher K. B., Weinberg D. H., 1995, MNRAS, 275, 515
Colless M. et al., 2001, MNRAS, 328, 1039
Contreras S., Baugh C., Norberg P., Padilla N., 2013, MNRAS, 432, 2717
Crain R. A. et al., 2015, MNRAS, 450, 1937
Croton D. J. et al., 2006, MNRAS, 365, 11
Davis M., Peebles P. J. E., 1983, ApJ, 267, 465
Driver S. P., Robotham A. S. G., 2010, MNRAS, 407, 2131
Driver S. P. et al., 2011, MNRAS, 413, 971
Falck B., Koyama K., Zhao G.-B., 2015, J. Cosmol. Astropart. Phys., 2015, 049
Farrow D. J. et al., 2015, MNRAS, 454, 2120
Fisher K. B., 1995, ApJ, 448, 494
Fisher K. B., Davis M., Strauss M. A., Yahil A., Huchra J., 1994, MNRAS, 266, 50
Fontanot F., Puchwein E., Springel V., Bianchi D., 2013, MNRAS, 436, 2672
Foreman-Mackey D., Hogg D. W., Lang D., Goodman J., 2013, PASP, 125, 306
Geller M. J., Peebles P. J. E., 1973, ApJ, 184, 329
Gonzalez-Perez V., Lacey C. G., Baugh C. M., Lagos C. D. P., Helly J., Campbell D. J. R., Mitchell P. D., 2014, MNRAS, 439, 264
Guo Q., White S., Angulo R. E., Henriques B., Lemson G., Boylan-Kolchin M., Thomas P., Short C., 2013, MNRAS, 428, 1351
Guzzo L. et al., 2008, Nature, 451, 541
Hamilton A. J. S., 1992, ApJ, 385, L5
Hamilton A. J. S., 1993, ApJ, 417, 19
Hamilton A. J. S., Tegmark M., 2004, MNRAS, 349, 115
Harrison E. R., 1974, ApJ, 191, L51
Hawkins E. et al., 2003, MNRAS, 346, 78
Hellwing W. A., Barreira A., Frenk C. S., Li B., Cole S., 2014, Phys. Rev. Lett., 112, 221102

Holwerda B. et al., 2015, MNRAS, 449, 4277

Jing Y., Borner G., 2001a, MNRAS, 325, 1389

Jing Y. P., Borner G., 2001b, ApJ, 547, 545

Jing Y. P., Borner G., 2004, ApJ, 617, 782

Jing Y. P., Mo H. J., Borner G., 1998, ApJ, 494, 1

Juszkiewicz R., Fisher K. B., Szapudi I., 1998, ApJ, 504, L1

Juszkiewicz R., Springel V., Durrer R., 1999, ApJ, 518, L25 (JSD model)

Kaiser N., 1987, MNRAS, 227, 1

Kang X., Jing Y. P., Mo H. J., Borner G., 2005, ApJ, 631, 21

Keenan R. C., Barger A. J., Cowie L. L., 2013, ApJ, 775, 62

Landy S. D., 2002, ApJ, 567, L1

Landy S. D., Szalay A. S., 1993, ApJ, 412, 64

Landy S. D., Szalay A. S., Broadhurst T. J., 1998, ApJ, 494, L133

Lemson G., the Virgo Consortium, 2006, preprint (arXiv:astro-ph/0608019)

Li C., Jing Y. P., Kauffmann G., Borner G., White S. D. M., Cheng F. Z., 2006, MNRAS, 368, 37

Li C., Jing Y. P., Kauffmann G., Borner G., Kang X., Wang L., 2007, MNRAS, 376, 984

Liske J. et al., 2015, MNRAS, 452, 2087

Loveday J., Efstathiou G., Maddox S. J., Peterson B. A., 1996, ApJ, 468, 1

Loveday J. et al., 2012, MNRAS, 420, 1239

Loveday J. et al., 2015, MNRAS, 451, 1540

Magira H., Jing Y. P., Suto Y., 2000, ApJ, 528, 30

McAlpine S. et al., 2016, Astron. Comput., 15, 72

Merson A. I. et al., 2013, MNRAS, 429, 556

Mo H. J., Jing Y. P., Borner G., 1993, MNRAS, 264, 825

Norberg P., Baugh C. M., Gaztañaga E., Croton D. J., 2009, MNRAS, 396, 19

Peacock J. A., Dodds S. J., 1994, MNRAS, 267, 1020

Peacock J. A. et al., 2001, Nature, 410, 169

Peebles P. J. E., 1976a, Ap&SS, 45, 3

Peebles P. J. E., 1976b, ApJ, 205, L109

Peebles P. J. E., 1979, AJ, 84, 730

Peebles P. J. E., 1980, The Large-Scale Structure of the Universe. Princeton Univ. Press, Prineton, NJ

Peebles P. J. E., 1993, Principles of Physical Cosmology. Princeton Univ. Press, Prineton, NJ

Reid B. A., White M., 2011, MNRAS, 417, 1913

Saunders W., Rowan-Robinson M., Lawrence A., 1992, MNRAS, 258, 134

Schaye J. et al., 2015, MNRAS, 446, 521

Scoccimarro R., 2004, Phys. Rev. D, 70, 083007

Sheth R. K., 1996, MNRAS, 279, 1310

Slosar A., Seljak U., Tasitsiomi A., 2006, MNRAS, 366, 1455

Swanson M. E. C., Tegmark M., Hamilton A. J. S., Hill J. C., 2008, MNRAS, 387, 1391

Tinker J. L., Norberg P., Weinberg D. H., Warren M. S., 2007, ApJ, 659, 877

Tonry J. L., Blakeslee J. P., Ajhar E. A., Dressler A., 2000, ApJ, 530, 625

Uhlemann C., Kopp M., Haugg T., 2015, Phys. Rev. D, 92, 063004

Van Den Bosch F. C. et al., 2007, MNRAS, 376, 841

Whitbourn J. R., Shanks T., 2016, MNRAS, 459, 496

Winther H. A. et al., 2015, MNRAS, 454, 4208

York D. G. et al., 2000, AJ, 120, 1579

Zehavi I. et al., 2002, ApJ, 571, 172

Zheng Z. et al., 2005, ApJ, 633, 791

APPENDIX A: COMPARISON WITH PREVIOUS GAMA CLUSTERING MEASUREMENTS

A comparison of the projected correlation function for various sub-samples of GAMA galaxies from this work and from Farrow et al. (2015) is presented in Fig. A1. We select our samples using the same redshift and luminosity limits as specified for the largest samples in five $^{0.0}M_r$ absolute magnitude bins from the top of table 2 in Farrow et al. Agreement is excellent on all scales. We thus find that our independently determined survey mask and radial selection

Figure A1. Comparison of the projected correlation function for various sub-samples of GAMA galaxies. Blue circles show measurements from this work; green squares show the comparison from Farrow et al. (2015). Both sets of measurements have been divided by the reference power law used by Farrow et al. in their fig. 10 (viz $r_0 = 5.33\,h^{-1}$ Mpc, $\gamma = 1.81$).

function do not impact measurements of the projected correlation function, on which our PVD estimates are based.

APPENDIX B: ACCURACY OF PROJECTED AND REAL-SPACE CORRELATION FUNCTION ESTIMATES

We here test how accurately one can recover the projected, $w_p(r_\perp)$, and real space, $\xi_r(r)$, correlation functions from the two-dimensional redshift-space correlation function $\xi(r_\perp, r_\parallel)$, making use of the GAMA mock catalogues. Since these mock catalogues include cosmological redshift, due purely to Hubble expansion, as well as observed redshift, including the LOS component of peculiar velocity, one can obtain a direct estimate of $\xi_r(r)$ using equation (1), with galaxy coordinates determined using cosmological

Table B1. Testing estimates of $w_p(r_\perp)$ and $\xi_r(r)$ using 26 volume-limited mock catalogues. The first row gives the power-law parameters obtained directly from the direction-averaged correlation function calculated in real space, i.e. using cosmological redshifts. The remaining rows show results obtained by integrating $\xi(r_\perp, r_\parallel)$ up to different values of $r_{\parallel max}$ in equation (3). The first column gives the upper integration limit, $r_{\parallel max}$, the second and third columns the mean and standard deviation of the recovered power-law parameters γ and r_0. The fourth column (χ_d^2) gives the χ^2 residual (for 20 degrees of freedom) between the direct estimate of $\xi_r(r)$ using cosmological redshifts, and the non-parametric estimates obtained by inverting $w_p(r_\perp)$. The fifth column (χ_{pl}^2) gives the χ^2 residual (for 11 degrees of freedom) for the power-law fit to the non-parametric estimate.

$r_{\parallel max}$ (h^{-1} Mpc)	γ	r_0 (h^{-1} Mpc)	χ_d^2	χ_{pl}^2
Direct	1.84 ± 0.01	4.84 ± 0.24		60
10	1.86 ± 0.01	5.09 ± 0.23	141	22
20	1.85 ± 0.02	4.95 ± 0.31	20	29
30	1.86 ± 0.02	4.82 ± 0.33	14	27
40	1.87 ± 0.02	4.85 ± 0.32	10	20
50	1.87 ± 0.02	4.85 ± 0.34	11	17
60	1.86 ± 0.03	4.86 ± 0.37	12	17
100	1.88 ± 0.03	4.67 ± 0.39	12	15

Figure B1. Average real-space correlation function $\xi_r(r)$ measured from 26 mock catalogues using direction-averaged correlation function and cosmological redshifts (green squares) and estimated from projecting and inverting the two-dimensional correlation function (equations 3 and 4 with $r_{\parallel max} = 40\,h^{-1}$ Mpc, blue circles). Both sets of measurements have been divided by the power-law fit to the direct $\xi_r(r)$ measurement (viz $r_0 = 4.84\,h^{-1}$ Mpc, $\gamma = 1.84$).

redshift and counting galaxy and random pairs as a function of total separation.

Carrying out this procedure for each of our mock catalogues, we obtain a real-space correlation function well-described by a power-law $\xi_r(r) = (r/r_0)^{-\gamma}$ over the range of separations 0.01–5 h^{-1} Mpc with parameters given in Table B1.
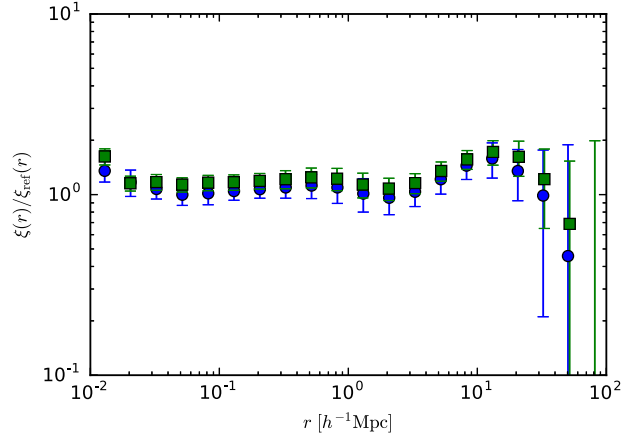
We then calculate the projected correlation function $w_p(r_\perp)$ for each of the mock catalogues as described in Section 3, fit a power law over the same range of scales, and use equation (5) to find the real-space power-law parameters r_0 and γ. We next invert $w_p(r_\perp)$ using equation (4) to obtain $\xi_r(r)$ estimates, and calculate the χ^2 residuals from the direct estimate. For both power-law fits and χ^2 estimates, we utilize the full covariance matrices of $w_p(r_\perp)$ and $\xi_r(r)$, respectively.

Our results, obtained using different values of $r_{\parallel max}$ in equation (3), are given in Table B1. These results show that the χ^2 residual between direct and indirect estimates of $\xi_r(r)$ is minimized for $r_{\parallel max} = 40\,h^{-1}$ Mpc. Moreover, power-law fits to $w_p(r_\perp)$ have converged by this point; therefore we use $r_{\parallel max} = 40\,h^{-1}$ Mpc when calculating $w_p(r_\perp)$ from the GAMA data.

In Fig. B1, we compare the real-space correlation function from the mock catalogues obtained directly using the cosmological redshifts, and using equations (3) and (4) with $r_{\parallel max} = 40\,h^{-1}$ Mpc. The deprojected correlation function is systematically lower than the directly measured one, but the bias is within the standard deviation of each measurement.

APPENDIX C: HAMILTON LINEAR INFALL EQUATIONS

Kaiser (1987) showed that coherent infall in Fourier space leads to a redshift-space power spectrum $P_s(k) = (1 + \beta\mu_k^2)P_r(k)$. Hamilton (1992) translated this into configuration space to show that the

redshift-space correlation function is given by

$$\xi'(r_\perp, r_\parallel) = \xi_0(s)P_0(\mu) + \xi_2(s)P_2(\mu) + \xi_4(s)P_4(\mu), \quad \text{(C1)}$$

where the $P_l(\mu)$ are Legendre polynomials. The harmonics of the correlation function are given by

$$\xi_0(s) = \left(1 + \frac{2\beta}{3} + \frac{\beta^2}{5}\right)\xi(r), \quad \text{(C2)}$$

$$\xi_2(s) = \left(\frac{4\beta}{3} + \frac{4\beta^2}{7}\right)[\xi(r) - \bar\xi(r)], \quad \text{(C3)}$$

$$\xi_4(s) = \frac{8\beta^2}{35}\left[\xi(r) + \frac{5}{2}\bar\xi(r) - \frac{7}{2}\bar{\bar\xi}(r)\right], \quad \text{(C4)}$$

where

$$\bar\xi(r) = \frac{3}{r^3}\int_0^r \xi(r')r'^2 dr', \quad \text{(C5)}$$

$$\bar{\bar\xi}(r) = \frac{5}{r^5}\int_0^r \xi(r')r'^4 dr'. \quad \text{(C6)}$$

For a power-law form for the correlation function, $\xi(r) = (r/r_0)^{-\gamma}$, equations (C2–C4) reduce to (Hawkins et al. 2003)

$$\xi_0(s) = \left(1 + \frac{2\beta}{3} + \frac{\beta^2}{5}\right)\xi(r), \quad \text{(C7)}$$

$$\xi_2(s) = \left(\frac{4\beta}{3} + \frac{4\beta^2}{7}\right)\left(\frac{\gamma}{\gamma - 3}\right)\xi(r), \quad \text{(C8)}$$

$$\xi_4(s) = \frac{8\beta^2}{35}\left[\frac{\gamma(2 + \gamma)}{(3 - \gamma)(5 - \gamma)}\right]\xi(r). \quad \text{(C9)}$$

This paper has been typeset from a TeX/LaTeX file prepared by the author.